

Lorentz-boost-driven magneto-optics in a Dirac nodal-line semimetal

J. Wyzula,¹ X. Lu,² D. Santos-Cottin,³ D. K. Mukherjee,^{2,4} I. Mohelský,¹ F. Le Mardelé,³ J. Novák,⁵ M. Novak,⁶ R. Sankar,⁷ Y. Krupko,^{1,8} B. A. Piot,¹ W.-L. Lee,⁷ A. Akrap,³ M. Potemski,^{1,9} M. O. Goerbig,² and M. Orlita^{1,10,*}

¹LNCMI-EMFL, CNRS UPR3228, Univ. Grenoble Alpes, Univ. Toulouse,
Univ. Toulouse 3, INSA-T, Grenoble and Toulouse, France

²Laboratoire de Physique des Solides, Université Paris Saclay,
CNRS UMR 8502, F-91405 Orsay Cedex, France

³Department of Physics, University of Fribourg, Chemin du Musée 3, 1700 Fribourg, Switzerland

⁴Department of Physics, Indiana University, Bloomington, Indiana 47405, USA

⁵Department of Condensed Matter Physics, Masaryk University, Kotlářská 2, 611 37 Brno, Czech Republic

⁶Department of Physics, Faculty of Science, University of Zagreb, 10000 Zagreb, Croatia

⁷Institute of Physics, Academia Sinica, Nankang, 11529 Taipei, Taiwan

⁸Institut d'Electronique et des Systemes, UMR CNRS 5214,

Université de Montpellier, 34000, Montpellier, France

⁹Institute of Experimental Physics, Faculty of Physics,
University of Warsaw, ul. Pasteura 5, 02-093 Warszawa, Poland

¹⁰Charles University, Faculty of Mathematics and Physics,
Institute of Physics, Ke Karlovu 5, 121 16 Prague 2, Czech Republic

Optical response of crystalline solids is to a large extent driven by excitations that promote electrons among individual bands. This allows one to apply optical and magneto-optical methods to determine experimentally the energy band gap – a fundamental property crucial to our understanding of any solid – with a great precision. Here we show that such conventional methods, applied with great success to many materials in the past, do not work in topological Dirac semimetals with a dispersive nodal line. There, the optically deduced band gap depends on how the magnetic field is oriented with respect to the crystal axes. Such highly unusual behaviour is explained in terms of band-gap renormalization driven by Lorentz boosts which results from the Lorentz-covariant form of the Dirac Hamiltonian relevant for the nodal line at low energies.

INTRODUCTION

Ever since the advent of graphene and topological materials, relativistic physics has become an integral part of condensed-matter sciences [1–3]. While emergent, it is important to stress that this type of relativity is pertinent beyond the dispersion of the low-energy excitations in many different solids. Klein tunneling [4–6] and the chiral anomaly [7–14] represent well-known examples. One of the salient aspects of relativity is the particular dependence of energy on the frame of reference: for a particle of mass m moving at a speed u lower than the speed of light c , a Lorentz boost to the comoving frame of reference changes the particle's energy from E to $E/\gamma = mc^2$, in terms of the Lorentz factor $\gamma = 1/\sqrt{1 - \beta^2}$ and the rapidity $\beta = u/c$. A natural question that one may now ask is the following: can one observe this relativistic renormalization equally in topological materials governed by the Dirac Hamiltonian or a variant of it, upon the replacement of c by a characteristic velocity v ?

While the effects of Lorentz covariance have been theoretically studied, namely in the framework of systems with tilted conical bands, both in two [15–17] and three [18–20] dimensions, an experimental verification is yet lacking. The key finding of this paper is that Lorentz boosts have important experimental consequences in Dirac materials. Most notably and unexpect-

edly, we find that the optical band gap extracted from magneto-optical measurements in the dispersive nodal-line Dirac semimetal niobium diarsenide (NbAs₂) depends on the orientation of the explored crystal. As we show below, this orientation defines a particular Lorentz boost, by fixing the angle between the applied magnetic field and the direction of the spectroscopically relevant part of the nodal line.

To appreciate the link between magnetic-field and Lorentz boosts in tilted cones, let us first consider a 2D conical band, characterized by a gap 2Δ and an asymptotic velocity v , which is tilted by an additional velocity parameter \mathbf{u} (in **Figure 1a**, $\mathbf{u} \parallel \hat{\mathbf{x}}$). Such a system is described by the following variant of a 2D massive Dirac Hamiltonian:

$$\hat{H}_{2D} = \hbar \mathbf{u} \cdot \mathbf{k} \mathbb{1} + \begin{bmatrix} \Delta & \hbar v(k_x - ik_y) \\ \hbar v(k_x + ik_y) & -\Delta \end{bmatrix}. \quad (1)$$

In an out-of-plane magnetic field, *i.e.*, with \mathbf{B} applied perpendicular to the x - y plane, and thus also to \mathbf{u} , the tilt can be formally viewed as a drift velocity of electrons in the crossed magnetic and effective electric fields, $\mathcal{E} = uB$. The drift is in the direction perpendicular to both the tilt and the magnetic field.

In this specific case, the problem of the electron motion in a tilted cone becomes mathematically equivalent to the

dynamics of a relativistic charge carrier in the crossed electric and magnetic fields [16, 19, 21]. This motion is therefore governed by fully Lorentz-covariant Dirac and Maxwell equations. This covariant formulation, and thus the use of Lorentz transformations, allows us to calculate the energy spectrum in a reference frame where the (effective) electric field vanishes, meaning $u = 0$ [16, 17, 21]. A similar relativistic-like approach has been invoked in the past, in order to understand behaviour of narrow-gap semiconductors [22–24] in real crossed electric and magnetic fields.

The impact of the tilt \mathbf{u} – or in the sense of reasoning above, the impact of the Lorentz boost – on the Landau quantization is profound [16, 19]. We obtain the Landau level (LL) spectrum that is typical of 2D massive Dirac electrons, but whose energy band gap and velocity parameter are renormalized by the Lorentz factor, $\gamma = 1/\sqrt{1 - u^2/v^2}$:

$$E_n = \pm \sqrt{(\Delta/\gamma)^2 + 2eBn\hbar v^2/\gamma^3}, \quad n = 0, 1, 2, \dots \quad (2)$$

For large tilts, $u \geq v$, the spectrum collapses and marks a transition between regimes referred to as magnetic and electric [19, 25]. In the semi-classical picture, this crossover corresponds to a transition from closed towards open cyclotron orbits in type-I and type-II conical bands (Figure 1a).

OPTICAL AND MAGNETO-OPTICAL RESPONSE OF NBAS₂

Let us now discuss how a Lorentz boost allows us to understand the magneto-optical response of NbAs₂ which is a nearly compensated 3D nodal-line semimetal [27] with a monoclinic crystal lattice and the space group C2/m [28]. Theory and experimental studies performed so far [26, 27] indicate the existence of two nodal lines in this material. Following a strict definition, these are 1D objects (curves) in momentum space, \mathbf{k}_{line} , along which the gap vanishes. Nevertheless, due to spin-orbit interaction, the gap does not close completely in NbAs₂. Instead, it only reaches a local minimum, similar to all other materials which are in current literature referred to as nodal-line or nodal-loop semimetals [29–31]. In NbAs₂, the nodal lines are open (periodically penetrating the Brillouin zone boundaries), they propagate approximately along the a crystallographic axis, and they are located symmetrically with respect to the Γ -Y-Z mirror plane (Figure 1b).

The low-energy electronic excitations around the nodal line can be described using a model for 2D massive Dirac electrons in the plane perpendicular to the local nodal-line direction $\boldsymbol{\tau}$ (left panel of Figure 1a). The corresponding velocity parameter v and the spin-orbit gap 2Δ vary smoothly along the line. Essentially for this work, the

nodal lines in NbAs₂ disperse with momentum and each approaches the Fermi energy four times within the Brillouin zone (Figure 1b,c). The crossings come in pairs of two different types. One of them is associated with a dispersive and the other one with a flat part [26]. They are located at $\mathbf{k}_{\text{line}}^D$ and $\mathbf{k}_{\text{line}}^F$, respectively, and characterized by the local directions $\boldsymbol{\tau}_D$ and $\boldsymbol{\tau}_F$ (Figure 1b,c).

In the absence of a magnetic field, the case we examine first, the optical response of NbAs₂ at low photon energies comprises direct signatures of nodal lines [26, 32, 33]. Two steps are clearly visible at the onset of interband absorption in the optical conductivity (Figure 1d down). They correspond to the local band gaps: $2\Delta_D = (88 \pm 2)$ meV and $2\Delta_F = (113 \pm 2)$ meV, at the dispersive and flat parts, respectively. Above this onset, the optical conductivity increases linearly in ω . While such behavior resembles systems with 3D conical bands [34–36], in NbAs₂, it is due to the occupation effect (Pauli-blocking) along the dispersive part of the nodal line [26, 32, 37, 38]. The anisotropy of the optical response (Figure 1d) reflects the orientation of the nodal lines, implying significantly higher Drude-type and interband absorption strength for the radiation polarized along the b axis which is approximately perpendicular to $\boldsymbol{\tau}$ [26]. Strong anisotropy, implying notably elongated Fermi surfaces, was also observed in magneto-transport experiments [33, 39–41].

To explore the magneto-optical response, we have identified a number of crystallographic facets on several NbAs₂ monocrystals using the standard x -ray technique [33]. Then, a series of infrared reflectivity measurements has been carried out, using non-polarized radiation and the Faraday configuration. The magnetic field was applied perpendicular to chosen crystallographic planes. In this way, we probed electrons undergoing cyclotron motion in crystallographic planes with various orientations with respect to the local nodal-line directions $\boldsymbol{\tau}_D$ and $\boldsymbol{\tau}_F$. To keep the geometry as simple as possible, we selected facets with a zero middle index ($n0m$). Thus the vector \mathbf{B} always lied in the mirror plane of the NbAs₂ crystals and formed identical angles θ_F and θ_D with the local directions, $\boldsymbol{\tau}_F$ and $\boldsymbol{\tau}_D$, of the two mirror-symmetric nodal lines at the flat and dispersive parts, respectively, where the Fermi level is crossed.

The relative magneto-reflectivity of NbAs₂, R_B/R_0 , measured with \mathbf{B} applied perpendicular to the (101), (201), (100), (20 $\bar{1}$) and (001) crystallographic planes, is presented in Figure 2a-e in a form of false-color plots. For illustration, we also append two stack-plots of selected reflectivity spectra collected on the (20 $\bar{1}$) and (001) facets in Figures 2f and g, respectively. Data measured on other facets are shown in Supplementary Materials [33]. The observed response contains a series of well-defined resonances with a weakly sublinear dependence on B that can be directly associated with interband inter-Landau-

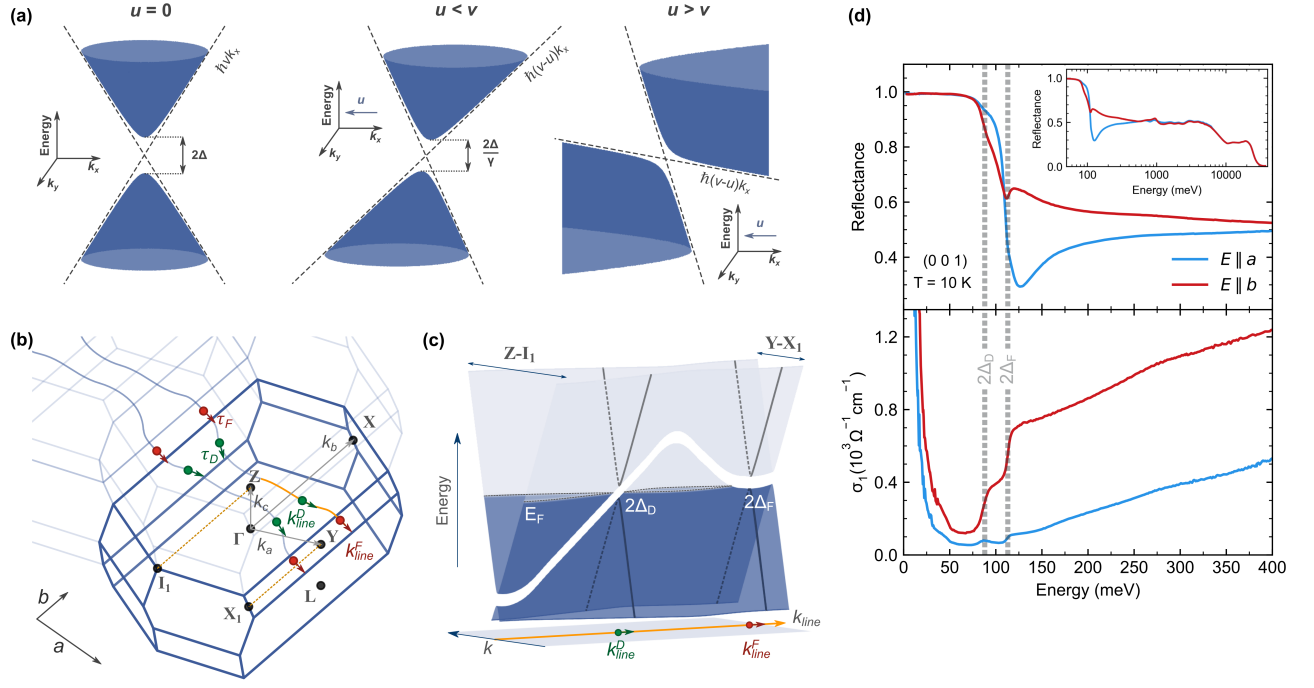


FIG. 1. (a) Hyperbolic dispersion of massive Dirac electrons with an additional tilt: $E(\mathbf{k}) = -\hbar u k_x \pm \sqrt{\Delta^2 + \hbar^2 v^2 k^2}$. (b) BZ of NbAs₂ with selected high-symmetry points. The blue curved lines show approximate positions of two nodal lines [26]. The crossings with the Fermi level are marked by green and red full circles, the arrows indicate local nodal-line directions, (c) Schematic view of the nodal line dispersion along the direction of propagation in a half of the BZ, highlighted using yellow color in panel (b). The band gaps at the crossing points with the Fermi energy are $2\Delta_D$ and $2\Delta_F$, for the dispersive and (approximately) flat parts of the nodal line, respectively. (d) Infrared reflectivity, and the extracted optical conductivity, measured on (001)-oriented facet of NbAs₂, using light polarized along the a and b axes.

level (inter-LL) excitations. The observed response – in position, spacing and relative/absolute intensity of inter-LL transitions – strongly varies with the explored facet. Across the board, this response includes two characteristic sets of interband inter-LL excitations: (i) the upper set, with transitions that always extrapolate to the energy of $2\Delta_F$ in the zero-field limit and are thus clearly associated with the flat crossing of the nodal line and (ii) the lower set of transitions that extrapolate, depending on the particular facet, to the energy equal to, or lower than $2\Delta_D$ (see $B = 0$ extrapolations using yellow dashed lines in Figure 2). For some facets, only one of these two sets is clearly manifested in the data.

This observation – an orientation-dependent gap – is the main finding of our work and it ventures beyond the common knowledge in LL spectroscopy of solids [42]. In conventional materials, the slope $d(\hbar\omega)/dB$, and the spacing of inter-LL excitations may depend on the orientation of the crystal with respect to the magnetic field, as well as on the experimental configuration (e.g., Faraday versus Voigt). Nevertheless, the apparent band gap obtained from the zero-field extrapolation of interband inter-LL excitations is widely used as an unambiguous estimate of the separation between electronic bands. Quite

unexpectedly, such an apparently evident approach fails in our case here.

THEORETICAL MODEL

To show that this orientation-dependent gap is a signature of the relativistic properties in the present material, let us consider the following minimal Hamiltonian for a dispersive nodal line:

$$\hat{H} = \hbar w q_{\text{line}} \mathbb{1} + \begin{bmatrix} \Delta & \hbar v(q_x - iq_y) \\ \hbar v(q_x + iq_y) & -\Delta \end{bmatrix}, \quad (3)$$

where the wave vector $\mathbf{q} = (q_x, q_y, q_{\text{line}}) = \mathbf{k} - \mathbf{k}_{\text{line}}$ is defined with respect to any point \mathbf{k}_{line} on the nodal line. The velocity parameter w describes the slope of the dispersing nodal line. In the plane (q_x, q_y) perpendicular to the local direction $\boldsymbol{\tau}$, the Hamiltonian (3) becomes that of a 2D massive Dirac electron, with the gap 2Δ and the asymptotic velocity v . In contrast, when the bands are cut in a plane that is not perpendicular to $\boldsymbol{\tau}$, the corresponding dispersion shows the tilt described by the Hamiltonian (1) and schematically shown in Figure 1a.

When a magnetic field is applied, making an angle θ with the local direction $\boldsymbol{\tau}$, it is the conventional Lorentz

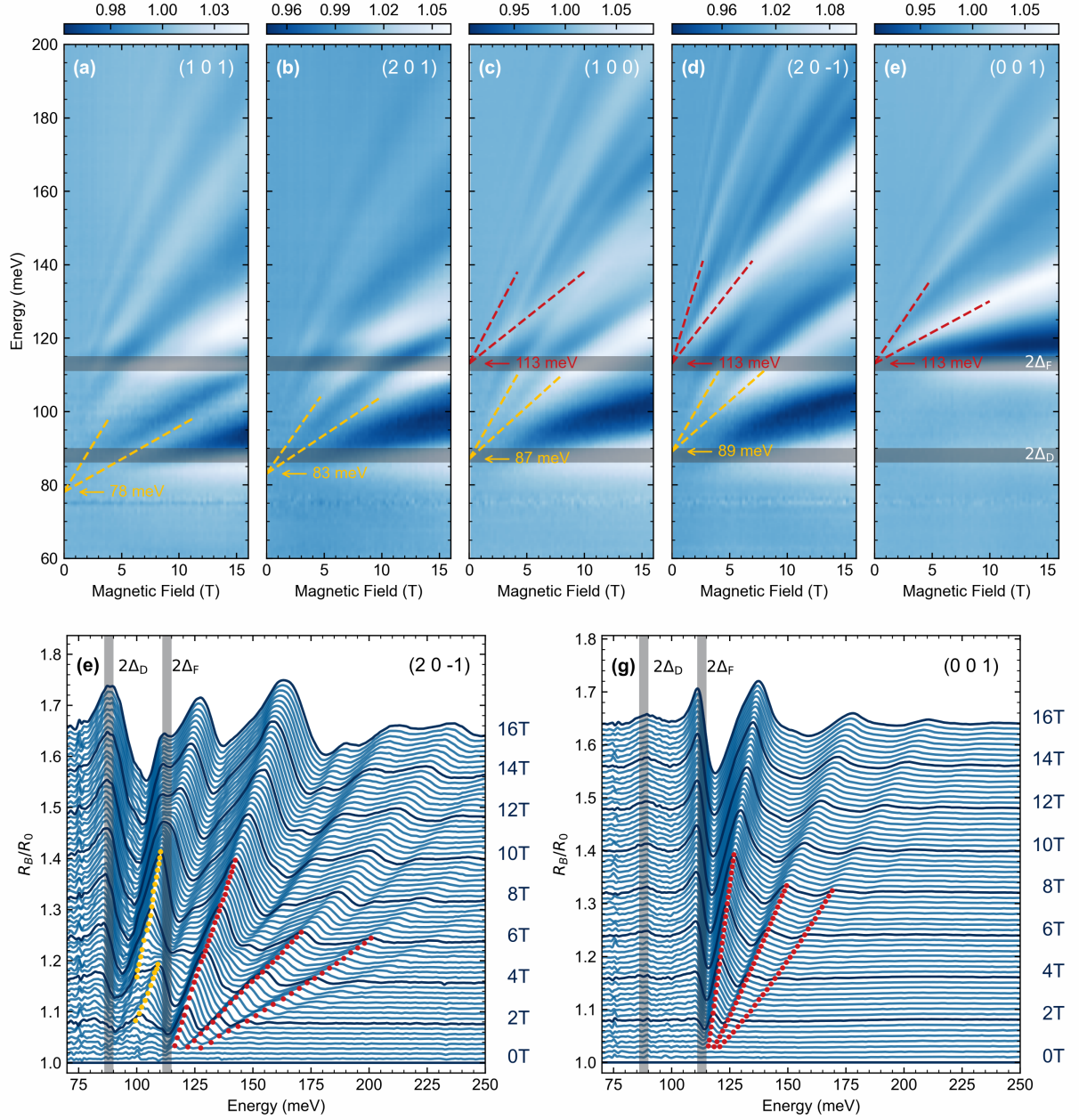


FIG. 2. Panels a-e: False color-plots of relative magneto-reflectivity of NbAs₂, R_B/R_0 , in the magnetic field applied along five different reciprocal space directions: (101), (201), (100), (20 $\bar{1}$) and (001), which make angles 62°, 51°, 29°, 7° and 90° with the a axis, respectively. The yellow and red values indicate the apparent optical band gaps, $2\Delta_D^{\text{eff}}$ and $2\Delta_F$, deduced using a linear zero-field extrapolation of inter-LL resonances belonging to the lower and upper set, respectively (dashed lines). Panels f and g: stack-plots of relative magneto-reflectivity spectra, R_B/R_0 , for selected values of the magnetic field collected on the (20 $\bar{1}$) and (001) facets, respectively. The yellow and red dots show R_B/R_0 maxima belonging to transitions in the lower and upper set, respectively. The horizontal and vertical gray bars show positions of the two steps in the onset of interband absorption at $2\Delta_D$ and $2\Delta_F$ at $B = 0$ (Figure 1d).

force and the particular profile of the dispersion which govern the motion of electrons in the plane perpendicular to \mathbf{B} . Thus, for non-zero angles θ , we study the magneto-optical response of electrons in tilted anisotropic conical bands, for details see Supplementary Materials [33]. The

corresponding LL spectrum then gets the Lorentz-boost-renormalized form of Equation 2, amended by the dispersive term $\hbar w_{QB}/\cos\theta$, where w_{QB} is the wave vector along the applied magnetic field. The rapidity determining the Lorentz factor is calculated as the ratio of the tilt and

asymptotic velocities, $w \sin \theta$ and $v \cos \theta$, respectively, so that $\beta = (w/v) \tan \theta$ [33]. Hence, depending on the orientation of the magnetic field with respect to the nodal line, we expect a pseudo-relativistic decrease of the band gap and the velocity parameter:

$$2\Delta \rightarrow 2\Delta^{\text{eff}} = \frac{2\Delta}{\gamma} \quad \text{and} \quad v \rightarrow v^{\text{eff}} = \frac{v\sqrt{\cos \theta}}{\gamma^{3/2}}, \quad (4)$$

in terms of the effective Lorentz factor:

$$\gamma = \frac{1}{\sqrt{1 - \frac{w^2}{v^2} \tan^2 \theta}}. \quad (5)$$

For angles exceeding the critical value of $\tan^{-1}(v/w)$, the quantization into LLs is expected to collapse in a way analogous to overtilted 3D conical bands [19]. Compared to 2D Dirac systems, Equation (5) clearly shows that the Lorentz factor γ is now tunable by the angle θ . This allows us to continuously monitor, using the angle θ , the band gap renormalization until the extinction of discrete LLs (see Figure 2).

DATA ANALYSIS AND DISCUSSION

To analyze our experimental data quantitatively in view of the above theoretical picture, we focus on the lowest observed line in both sets and assign it to the inter-LL excitation $0 \leftrightarrow 1$. Even though the pseudo-relativistic renormalization may profoundly alter the selection rules [17, 33], this transition is theoretically [33] expected to remain strong for any $\beta < 1$ and its energy reads:

$$\hbar\omega_{0 \leftrightarrow 1} = \Delta^{\text{eff}} + \sqrt{(\Delta^{\text{eff}})^2 + 2\hbar B(v^{\text{eff}})^2}. \quad (6)$$

This expression, as well as Equations (4) and (5) are valid for both optically active parts of the nodal line. In the flat part around $\mathbf{k}_{\text{line}}^F$, we have $w = 0$, i.e., $\gamma = 1$, so that one does not expect any facet dependence of the associated optical gap. In contrast, one expects a facet-dependent pseudo-relativistic decrease of the optical gap associated with the dispersive part around $\mathbf{k}_{\text{line}}^D$.

These expectations are indeed corroborated by our magneto-optical measurements. In our data analysis, we associate the maxima in R_B/R_0 spectra with positions of inter-LL excitations, a solid assumption in the vicinity of the plasma edge (cf. Figure 1d and [33]). The effective values of the band gap and velocity parameter derived for all explored facets are presented in **Figure 3a-d**. The response of the flat part matches perfectly the expectations for a Landau-quantized 2D massive Dirac system. The effective band gap $2\Delta_F^{\text{eff}} = (113 \pm 2)$ meV stays constant within the experimental error (Figure 3a). The variation of the effective velocity (Figure 3b) with the facet

reflects the geometrical factor, $v_F^{\text{eff}} = v_F \sqrt{\cos \theta_F}$, where $v_F = (6.3 \pm 0.3) \times 10^5$ m/s, due to mutual orientation of \mathbf{B} and $\boldsymbol{\tau}_F$. This allows us to deduce the local direction of the flat part. The best agreement has been found for $\boldsymbol{\tau}_F$ in the mirror a - c plane, $(0 \pm 2)^\circ$, but inclined by $(-23 \pm 2)^\circ$ from the $(a$ - b) plane, in perfect agreement with conclusions reached by Shao et al. [26]. Notably, for some explored facets, the angle θ_F approaches 90° and the upper set of inter-LL excitations can no longer be distinguished in the magneto-reflectivity data (see, e.g., Figure 2a,b).

In contrast, the effective gap $2\Delta_D^{\text{eff}}$ deduced for the dispersive part spreads over an interval greater than 10 meV (Figure 3c). To compare this behaviour with our Lorentz-boost-induced gap renormalization (4), we have minimized the difference between the theoretical expectations and experimental values of the effective gap and velocity, deduced for all facets, by varying parameters Δ_D , v_D , w as well as the local direction $\boldsymbol{\tau}_D$. A very good agreement was obtained (dashed lines in Figure 3c,d) for the following parameters: $v_D = (5.3 \pm 0.5) \times 10^5$ m/s, $w = (1.5 \pm 0.5) \times 10^5$ m/s, $2\Delta_D = (89 \pm 2)$ meV, and the local direction $\boldsymbol{\tau}_D$ that deviates by $(25 \pm 10)^\circ$ from the mirror $(a$ - c) plane and by $(-5 \pm 2)^\circ$ from the a - b plane. These parameters agree well with the previous estimates given by Shao et al. [26]. Slightly larger values were found for w and the angle of $\boldsymbol{\tau}_D$ with respect to the a - c plane. Importantly, the angle θ_D reaches larger values for certain explored facets, thus implying a rapidity that exceeds unity. In such cases, the lower set of inter-LL excitations disappears entirely from the magneto-optical response, suggesting the complete collapse of the LL spectrum. This happens for the data collected on the (001)-oriented facet ($\theta_D \approx 85^\circ$) presented in Figure 2d, and also the (203)-oriented facet ($\theta_D \approx 64^\circ$), see Supplementary Materials [33].

In addition to the Lorentz-boost renormalization of the spectrum, our model for the dispersive nodal line implies a departure from the conventional electric-dipole selection rules, $n \rightarrow n \pm 1$, which are generally valid for all isotropic systems [42]. To illustrate this, we have numerically evaluated the matrix elements for electric-dipole interband excitations between different pairs of LLs ($n = 0 \dots 6$) and visualized them graphically in Figure 3e. We have chosen two particular angles, $\theta_D = 61^\circ$ and 28° , which correspond to the magnetic field oriented perpendicular to the (101) and (201) planes, respectively. For small angles θ_D , the magneto-optical response is dominated by $n \rightarrow n \pm 1$ transitions, although other excitations emerge as well (e.g., $n \rightarrow n \pm 2$). In contrast, for larger angles θ_D , one finds a plethora of optical transitions. The dominant ones follow the rule-of-thumb selection rules $n \rightarrow \alpha n$ and $n \rightarrow n/\alpha$, where α is an integer ($\alpha = 4-6$ in the left panel of Figure 3e), in agreement with preceding works on tilted 3D cones [17, 19]. This re-

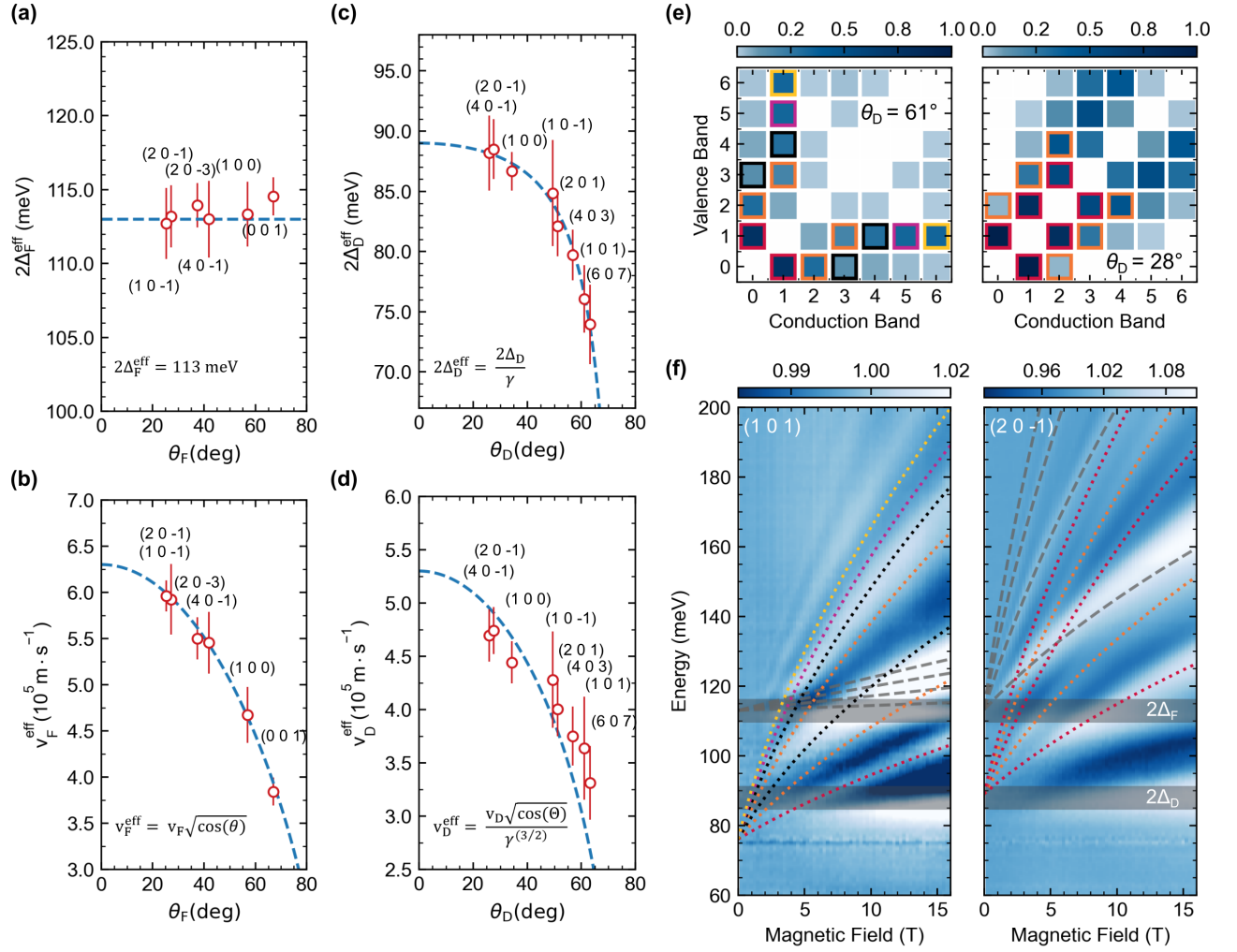


FIG. 3. Effective band gap and velocity parameter obtained by a fit of the massive-Dirac model to the lowest inter-LL transition in sets belonging to the flat and dispersive crossings with the Fermi energy: (a),(b) and (c),(d), respectively. (e) Absolute values of matrix elements (the darker color, the stronger the transition) for electric-dipole inter-LL interband excitations (for LLs $n = 0 \dots 6$ in both conduction and valence bands) calculated for $2\Delta_D = 89$ meV, $v_D = 5.3 \times 10^5$ m/s, $w = 1.5 \times 10^5$ m/s and for two different angles $\theta_D = 61^\circ$ and 28° between τ_D and \mathbf{B} . These two angles correspond to the configuration with \mathbf{B} perpendicular to the crystallographic planes (101) and (20 $\bar{1}$), respectively, for which the experimental R_B/R_0 traces are plotted in (f) in a form of false-color plots. The dotted lines show selected inter-LL excitations from the dispersive part of the nodal line, assumed to be electric-dipole active based on the matrix elements presented in (e). We use the same color-framing/coding in (e) and (f) to facilitate the identification of individual transitions. For instance, the lowest (red-dotted) line in (f) corresponds to the $0 \leftrightarrow 1$ transitions. The gray dashed lines show the expected transitions in the flat part (selection rules $n \rightarrow n \pm 1$, for $v_F = 6.3 \times 10^5$ m/s and $\Delta_F = 113$ meV).

sult may be understood in a broader context of materials which do not have a full rotational symmetry along the direction of the applied magnetic field and in which inter-LL excitations beyond the basic selection rules $n \rightarrow n \pm 1$ become electric-dipole active [43, 44].

As seen in Figure 3e, the lowest energy transitions $1 \leftrightarrow 0$ stay strong as long as $\beta < 1$ and were used to deduce the effective parameters $2\Delta_D^{\text{eff}}$ and v_D^{eff} . These parameters may now, in turn, be used to identify excitations between LLs with higher indices and thus get ex-

perimental insights into the selection rules. To this end, we compare in Figure 3f the experimental data collected with \mathbf{B} perpendicular to the (101) and (20 $\bar{1}$) crystallographic planes, with the expected positions of selected interband inter-LL excitations (dotted lines) calculated using the corresponding effective gap and velocity parameters. To facilitate the comparison, we use the color-framing/coding introduced in Figure 3e. In line with our expectations, we identify $n \rightarrow n \pm 1$ and $n \rightarrow n \pm 2$ excitations in the response on the (20 $\bar{1}$)-oriented facet which

implies a relatively small angle θ_D (Figure 3f right). In contrast, when the magnetic field is applied perpendicularly to the (101) crystallographic plane (Figure 3f left), we identify transitions with a greater change of the LL index, such as $1 \rightarrow 4$ or $1 \rightarrow 3$, and no line following the standard $n \rightarrow n \pm 1$ selection rule is found, except for the lowest one, $0 \leftrightarrow 1$. In both cases, the gray dashed lines show the expected response of the flat part of the nodal line that follow the standard $n \rightarrow n \pm 1$ selection rules and no additional excitations emerge, unlike in the dispersive part.

CONCLUSIONS

We have found that the optical band gap of the nodal-line semimetal NbAs₂ measured via magneto-optical spectroscopy depends on the facet explored in the experiment. This observation is understood as a consequence of the pseudo-relativistic renormalization of the band gap within a Lorentz boost determined by the slope of the dispersive nodal line. The slope defines, together with the direction of the applied magnetic field, the tilt of the conical dispersion of a massive 2D Dirac electron in the plane perpendicular to the applied magnetic field. Our findings show that the emergent relativistic description of topological quantum materials in terms of Dirac Hamiltonians, or its variants, as well as the use of Lorentz transformations can be pushed surprisingly far. The observed Lorentz-boost-driven renormalization can be also viewed as an analogue of the well-known Franz-Keldysh effect in the magnetic field [22, 45], nevertheless, in our case, with no real electric field applied.

EXPERIMENTAL SECTION

Sample growth and characterization

NbAs₂ single crystals explored in this work were grown using a chemical vapor transport method. The as-grown crystals usually have a several facets with different crystallographic orientations with shiny surfaces suitable for infrared reflectivity experiments. Individual facets were identified using conventional *x*-ray technique, using a diffractometer equipped with Cu *x*-ray tube, channel-cut germanium monochromator and scintillation detector.

Optical spectroscopy at $B = 0$

To deduce the optical conductivity of NbAs₂ in Figure 1d, the reflectivity on the (001)-oriented facet was measured using radiation polarized linearly along the *a* and *b* crystallographic axes. To this end, the Vertex 70v FTIR spectrometer was used, equipped with custom-built in-situ gold-evaporation technique. At high photon energies, the phase was fixed by ellipsometry. Then, the standard Kramers-Kronig analysis was employed to ob-

tain the frequency-dependent complex optical conductivity.

Infrared magneto-spectroscopy

The magneto-reflectivity of NbAs₂ was explored in the Faraday configuration, with **B** applied perpendicular to the chosen crystallographic plane. During experiments, a macroscopic area of the sample (typically a few mm²), placed in a superconducting coil and kept at $T = 4.2$ K in the helium exchange gas, was exposed to radiation of a globar, which was analyzed by the Vertex 80v FTIR spectrometer and delivered to the sample via light-pipe optics. The reflected light was detected by a liquid-helium-cooled bolometer placed outside the magnet. The reflectivity R_B recorded at a given magnetic field B was normalized by $R_{B=0}$. In addition, a baseline correction was performed to compensate for variation of the absolute signal intensity over time. To this end, relative magneto-transmission spectra, R_B/R_0 , were normalized to unity in the spectral range away around $\hbar\omega = 400$ meV or above (away from the range of interest). The reflectivity spectra on each facet were collected using the $\delta B = 0.25$ T steps. To create false-color plots of R_B/R_0 spectra in Figures 2a-e and 3f, no linear interpolation was used. Instead, the spectrum collected at the magnetic field of B was plotted in the interval of $B \pm \delta B/2$. To facilitate the data analysis, we assumed that the maxima in relative magneto-reflectivity, R_B/R_0 , directly correspond to the positions of inter-LL resonances. This is justified when the imaginary part of the dielectric function exceeds the absolute value of the real part – a condition fulfilled at photon energies around and slightly above the plasma edge (Figure 1d). A more detailed analysis indicates that, in this way, we slightly overestimate/underestimate the positions of resonances at lower/higher part of the explored range.

Supporting Information

Supporting Information is available from the Wiley Online Library or from the author.

Acknowledgements

We acknowledge discussions with T. Brauner and S. Tchoumakov. The work has been supported by the ANR DIRAC3D project (ANR-17-CE30-0023) and exchange programme PHC ORCHID (47044XE). A. A. acknowledges funding from the Swiss National Science Foundation through Project No. PP00P2-170544. M.N. acknowledges the support of CeNIKS project co-financed by the Croatian Government and the EU through the European Regional Development Fund - Competitiveness and Cohesion Operational Program (Grant No. KK.01.1.1.02.0013). R.S. acknowledges financial support provided by the Ministry of Science and Technology in Taiwan under project numbers MOST-110-2112-M-001-065-MY3 as well as Academia Sinica for the budget of AS-iMate-109-13. D.K.M. acknowledges partial support

from NSF Grant No. DMR-1914451, and the Research Corporation for Science Advancement through a Cottrell SEED award. This work was also supported by CNRS through IRP "TeraMIR" and by ANR Colector (ANR-19-CE30-0032). We also acknowledge the support of the LNCMI-CNRS in Grenoble, a member of the European Magnetic Field Laboratory (EMFL).

* milan.orlita@lncmi.cnrs.fr

- [1] A. Bansil, H. Lin, and T. Das, Colloquium: Topological band theory, *Rev. Mod. Phys.* **88**, 021004 (2016).
- [2] C.-K. Chiu, J. C. Y. Teo, A. P. Schnyder, and S. Ryu, Classification of topological quantum matter with symmetries, *Rev. Mod. Phys.* **88**, 035005 (2016).
- [3] N. P. Armitage, E. J. Mele, and A. Vishwanath, Weyl and Dirac semimetals in three-dimensional solids, *Rev. Mod. Phys.* **90**, 015001 (2018).
- [4] O. Klein, Die reflexion von elektronen an einem potenzsprung nach der relativistischen dynamik von Dirac, *Zeitschrift für Physik* **53**, 157 (1929).
- [5] M. I. Katsnelson, K. S. Novoselov, and A. K. Geim, Chiral tunnelling and the Klein paradox in graphene, *Nature Phys.* **2**, 620 (2006).
- [6] A. F. Young and P. Kim, Quantum interference and Klein tunnelling in graphene heterojunctions, *Nature Phys.* **5**, 222 (2009).
- [7] H. B. Nielsen and M. Ninomiya, The Adler-Bell-Jackiw anomaly and Weyl fermions in a crystal, *Physics Letters B* **130**, 389 (1983).
- [8] D. T. Son and B. Z. Spivak, Chiral anomaly and classical negative magnetoresistance of Weyl metals, *Phys. Rev. B* **88**, 104412 (2013).
- [9] J. Xiong, S. K. Kushwaha, T. Liang, J. W. Krizan, M. Hirschberger, W. Wang, R. J. Cava, and N. P. Ong, Evidence for the chiral anomaly in the Dirac semimetal Na_3Bi , *Science* **350**, 413 (2015).
- [10] X. Huang, L. Zhao, Y. Long, P. Wang, D. Chen, Z. Yang, H. Liang, M. Xue, H. Weng, Z. Fang, X. Dai, and G. Chen, Observation of the chiral-anomaly-induced negative magnetoresistance in 3D Weyl semimetal TaAs , *Phys. Rev. X* **5**, 031023 (2015).
- [11] A. Burkov, Chiral anomaly without relativity, *Science* **350**, 378 (2015).
- [12] R. D. dos Reis, M. O. Ajeesh, N. Kumar, F. Arnold, C. Shekhar, M. Naumann, M. Schmidt, M. Nicklas, and E. Hassinger, On the search for the chiral anomaly in Weyl semimetals: the negative longitudinal magnetoresistance, *New J. Phys.* **18**, 085006 (2016).
- [13] S. Jia, S.-Y. Xu, and M. Z. Hasan, Weyl semimetals, Fermi arcs and chiral anomalies, *Nature Mater.* **15**, 1140 (2016).
- [14] N. P. Ong and S. Liang, Experimental signatures of the chiral anomaly in Dirac-Weyl semimetals, *Nature Rev. Phys.* **3**, 394 (2021).
- [15] S. Katayama, A. Kobayashi, and Y. Suzumura, Pressure-induced zero-gap semiconducting state in organic conductor α -(BEDT-TTF) $_2\text{I}_3$ salt, *Journal of the Physical Society of Japan* **75**, 054705 (2006).
- [16] M. O. Goerbig, J.-N. Fuchs, G. Montambaux, and F. Piéchon, Electric-field-induced lifting of the valley degeneracy in α -(BEDT-TTF) $_2\text{I}_3$ Dirac-like Landau levels, *EPL (Europhysics Letters)* **85**, 57005 (2009).
- [17] J. Sári, M. O. Goerbig, and C. Tóke, Magneto-optics of quasirelativistic electrons in graphene with an in-plane electric field and in tilted Dirac cones in α -(BEDT TTF) $_2\text{I}_3$, *Phys. Rev. B* **92**, 035306 (2015).
- [18] A. A. Soluyanov, D. Gresch, Z. Wang, Q. Wu, M. Troyer, X. Dai, and B. A. Bernevig, Type-II Weyl semimetals, *Nature* **527**, 495 (2015).
- [19] S. Tchoumakov, M. Civelli, and M. O. Goerbig, Magnetic-field-induced relativistic properties in type-I and type-II Weyl semimetals, *Phys. Rev. Lett.* **117**, 086402 (2016).
- [20] L. Zhang, Y. Jiang, D. Smirnov, and Z. Jiang, Landau quantization in tilted Weyl semimetals with broken symmetry, *J. Appl. Phys.* **129**, 105107 (2021).
- [21] V. Lukose, R. Shankar, and G. Baskaran, Novel electric field effects on Landau levels in graphene, *Phys. Rev. Lett.* **98**, 116802 (2007).
- [22] A. G. Aronov and G. E. Pikus, Light absorption in semiconductors in crossed electric and magnetic fields, *Soviet Physics JETP* **24**, 339 (1967).
- [23] W. Zawadzki, S. Klahn, and U. Merkt, Semirelativistic behavior of electrons in InSb in crossed magnetic and electric fields, *Phys. Rev. Lett.* **55**, 983 (1985).
- [24] W. Zawadzki, S. Klahn, and U. Merkt, Inversion electrons on narrow-band-gap semiconductors in crossed electric and magnetic fields, *Phys. Rev. B* **33**, 6916 (1986).
- [25] S. Takeuchi, Relativistic $E \times B$ acceleration, *Phys. Rev. E* **66**, 037402 (2002).
- [26] Y. Shao, Z. Sun, Y. Wang, C. Xu, R. Sankar, A. J. Breindel, C. Cao, M. M. Fogler, A. J. Millis, F. Chou, Z. Li, T. Timusk, M. B. Maple, and D. N. Basov, Optical signatures of Dirac nodal lines in NbAs_2 , *PNAS* **116**, 1168 (2019).
- [27] C. Xu, J. Chen, G.-X. Zhi, Y. Li, J. Dai, and C. Cao, Electronic structures of transition metal dipnictides XPn_2 ($X = \text{Ta, Nb}$; $\text{Pn} = \text{P, As, Sb}$), *Phys. Rev. B* **93**, 195106 (2016).
- [28] W. Bensch and W. Heid, NbAs_2 , *Acta Crystallographica Section C* **51**, 2205 (1995).
- [29] Y. Shao, A. N. Rudenko, J. Hu, Z. Sun, Y. Zhu, S. Moon, A. J. Millis, S. Yuan, A. I. Lichtenstein, D. Smirnov, et al., Electronic correlations in nodal-line semimetals, *Nature Phys.* **16**, 636 (2020).
- [30] L. M. Schoop, M. N. Ali, C. Straßer, A. Topp, A. Varykhalov, D. Marchenko, V. Duppel, S. S. P. Parkin, B. V. Lotsch, and C. R. Ast, Dirac cone protected by non-symmorphic symmetry and three-dimensional Dirac line node in ZrSiS , *Nature Comm.* **7**, 11696 (2016).
- [31] D. Takane, Z. Wang, S. Souma, K. Nakayama, C. X. Trang, T. Sato, T. Takahashi, and Y. Ando, Dirac-node arc in the topological line-node semimetal HfSiS , *Phys. Rev. B* **94**, 121108 (2016).
- [32] E. J. Mele, Dowsing for nodal lines in a topological semimetal, *PNAS* **116**, 1084 (2019).
- [33] See Supplementary Materials.
- [34] T. Timusk, J. P. Carbotte, C. C. Homes, D. N. Basov, and S. G. Sharapov, Three-dimensional Dirac fermions in quasicrystals as seen via optical conductivity, *Phys. Rev. B* **87**, 235121 (2013).
- [35] M. Orlita, D. M. Basko, M. S. Zholudev, F. Teppe,

- W. Knap, V. I. Gavrilenko, N. N. Mikhailov, S. A. Dvoretckii, P. Neugebauer, C. Faugeras, A.-L. Barra, G. Martinez, and M. Potemski, Observation of three-dimensional massless Kane fermions in a zinc-blende crystal, *Nature Phys.* **10**, 233 (2014).
- [36] D. Neubauer, J. P. Carbotte, A. A. Nateprov, A. Löhle, M. Dressel, and A. V. Pronin, Interband optical conductivity of the [001]-oriented Dirac semimetal Cd_3As_2 , *Phys. Rev. B* **93**, 121202 (2016).
- [37] A. V. Pronin and M. Dressel, Nodal semimetals: A survey on optical conductivity, *phys. stat. sol. (b)* **258**, 2000027 (2021).
- [38] D. Santos-Cottin, M. Casula, L. de' Medici, F. Le Mardelé, J. Wyzula, M. Orlita, Y. Klein, A. Gauzzi, A. Akrap, and R. P. S. M. Lobo, Optical conductivity signatures of open dirac nodal lines, *Physical Review B* **104**, L201115 (2021).
- [39] B. Shen, X. Deng, G. Kotliar, and N. Ni, Fermi surface topology and negative longitudinal magnetoresistance observed in the semimetal NbAs_2 , *Phys. Rev. B* **93**, 195119 (2016).
- [40] Y.-Y. Wang, Q.-H. Yu, P.-J. Guo, K. Liu, and T.-L. Xia, Resistivity plateau and extremely large magnetoresistance in NbAs_2 and TaAs_2 , *Phys. Rev. B* **94**, 041103 (2016).
- [41] G. Peramaiyan, R. Sankar, I. P. Muthuselvam, and W.-L. Lee, Anisotropic magnetotransport and extremely large magnetoresistance in NbAs_2 single crystals, *Sci. Rep.* **8**, 1 (2018).
- [42] G. Landwehr and E. I. Rashba, *Landau level spectroscopy* (Elsevier, 2012).
- [43] M. Orlita, P. Neugebauer, C. Faugeras, A.-L. Barra, M. Potemski, F. M. D. Pellegrino, and D. M. Basko, Cyclotron motion in the vicinity of a Lifshitz transition in graphite, *Phys. Rev. Lett.* **108**, 017602 (2012).
- [44] O. Ly and D. M. Basko, Theory of electron spin resonance in bulk topological insulators Bi_2Se_3 , Bi_2Te_3 and Sb_2Te_3 , *J. Phys.: Condens. Matter* **28**, 155801 (2016).
- [45] W. Franz, Einfluß eines elektrischen Feldes auf eine optische Absorptionskante, *Zeitschrift für Naturforschung A* **13**, 484 (1958).

Supplementary Information for "Lorentz-boost-driven magneto-optics in Dirac matter"

J. Wyzula,¹ X. Lu,² D. Santos-Cottin,³ D. K. Mukherjee,^{2,4} I. Mohelský,¹ F. Le Mardelé,³ J. Novák,⁵ M. Novak,⁶ R. Sankar,⁷ Y. Krupko,^{1,8} B. A. Piot,¹ W.-L. Lee,⁷ A. Akrap,³ M. Potemski,^{1,9} M. O. Goerbig,² and M. Orlita^{1,10,*}

¹*LNCMI-EMFL, CNRS UPR3228, Univ. Grenoble Alpes, Univ. Toulouse, Univ. Toulouse 3, INSA-T, Grenoble and Toulouse, France*

²*Laboratoire de Physique des Solides, Université Paris Saclay, CNRS UMR 8502, F-91405 Orsay Cedex, France*

³*Department of Physics, University of Fribourg, Chemin du Musée 3, 1700 Fribourg, Switzerland*

⁴*Department of Physics, Indiana University, Bloomington, Indiana 47405, USA*

⁵*Department of Condensed Matter Physics, Masaryk University, Kotlářská 2, 611 37 Brno, Czech Republic*

⁶*Department of Physics, Faculty of Science, University of Zagreb, 10000 Zagreb, Croatia*

⁷*Institute of Physics, Academia Sinica, Nankang, 11529 Taipei, Taiwan*

⁸*Institut d'Electronique et des Systemes, UMR CNRS 5214, Université de Montpellier, 34000, Montpellier, France*

⁹*Institute of Experimental Physics, Faculty of Physics, University of Warsaw, ul. Pasteura 5, 02-093 Warszawa, Poland*

¹⁰*Charles University, Faculty of Mathematics and Physics, Institute of Physics, Ke Karlovu 5, 121 16 Prague 2, Czech Republic*

CONTENTS

I. Sample growth and x-ray characterization	1
II. Optical response of NbAs ₂ at $B = 0$	2
III. Nodal lines in magnetic field	5
A. Landau levels	5
B. Velocity operators	7
C. Selection rules	7
IV. Infrared magneto-reflectivity technique and complementary magneto-optical data	9
V. Magneto-transport experiments	9
References	11

I. SAMPLE GROWTH AND X-RAY CHARACTERIZATION

NbAs₂ single crystals explored in this work were grown using a chemical vapor transport method. The as-grown crystals usually have a several facets with different crystallographic orientations with shiny surfaces suitable for infrared reflectivity experiments. In total, four NbAs₂ single crystal samples (No. 1...4) were used to collect the magneto-optical data presented in this work and characterized using standard x -ray technique. To this end, Bragg-Brentano diffractometer equipped with Cu x -ray tube, channel-cut germanium monochromator and scintillation detector were employed. The x -ray diffraction patterns of each explored sample and facet are presented in Fig. S1. For the purpose of optical experiments on the (001) facet at $B = 0$, the orientation a and b crystallographic axes was determined using pole diagrams. The magneto-reflectivity data with B oriented perpendicular to the (101) and (607) crystallographic planes were collected using the nearby (403) facet on Sample 1 rotated respectively by 5 and 7° in the (a - c) plane.

* milan.ortita@lncmi.cnrs.fr

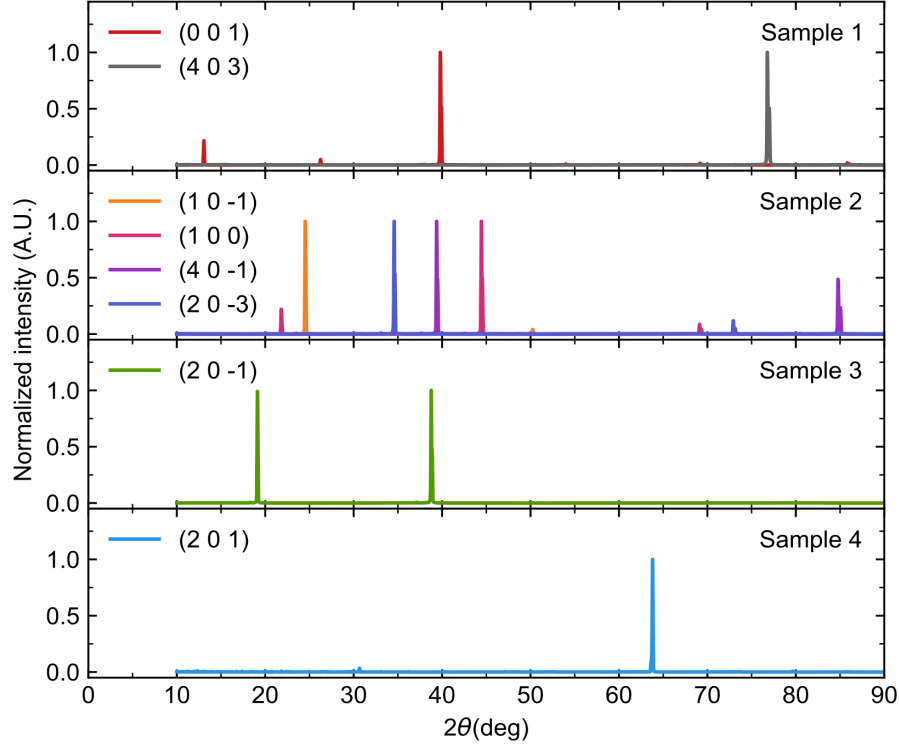


FIG. S1. Normalized diffraction patterns of all facets studied in our magneto-optical experiments. The (001)-oriented facet of Sample 1 was also used for reflectance measurements at $B = 0$.

II. OPTICAL RESPONSE OF NBAS₂ AT $B = 0$

To characterize the optical response of NbAs₂ at $B = 0$, infrared reflectivity was measured on the (001)-oriented facet using radiation polarized linearly along the a and b crystallographic axes. To this end, the Vertex 70v FTIR spectrometer was used, equipped with custom-built in situ gold evaporation. At high photon energies, the phase was fixed by ellipsometry. Then, the standard Kramers-Kronig analysis was employed to obtain the frequency-dependent complex optical conductivity. The measured reflectivity and the deduced optical conductivity are presented in Fig. 1d in the main part of the manuscript and in Figs. S3a,c,e.

To describe the optical response of NbAs₂ at $B = 0$ theoretically, we use the simple model for electronic states in a nodal-line semimetal proposed in the main text. The proposed Hamiltonian, now with both line index $\xi = \pm 1$ and spin included, reads:

$$\hat{H} = (\varepsilon_0 + \hbar w q_{\text{line}}) \mathbb{1} + \hbar v (\xi q_x \sigma_x + q_y \sigma_y) + \xi \Delta \sigma_z \tau_z, \quad (\text{S1})$$

where σ_i ($i = x, y, z$) and τ_z are standard Pauli matrices for orbital and spin degrees of freedom, respectively. This Hamiltonian describes electronic states in the vicinity of any point at the nodal line, $\mathbf{k} = \mathbf{k}_{\text{line}} + \mathbf{q}$. The used orthogonal coordinate system, $\mathbf{q} = (q_x, q_y, q_{\text{line}} \equiv q_z)$, has the third component always aligned with the local direction of the nodal line $\boldsymbol{\tau}$ (see Fig. S2) which is roughly parallel with the a crystallographic axis [1]. The other nodal line is located symmetrically in momentum space with respect to the Γ -Y-Z mirror plane. Similar to the local direction $\boldsymbol{\tau}$, the Hamiltonian parameters ε_0 , v , Δ and w also vary, smoothly and weakly along the nodal line, and therefore, can be viewed as a function of q_{line} .

To simplify the problem at hand, we have divided the nodal line zone into four segments I, II, III and IV, which approximately describe its propagation through a half of the Brillouin zone. The locations of these segments, as well as their conduction/valence band energies (at \mathbf{k}_{line}), are shown in Figs. S3b,d,f. The suggested profile of the nodal lines approach the results of DFT simulations and overall conclusions presented by Shao et al.[1]. In each segment, the nodal line is reduced down to a straight line in momentum space – having the length of k^i – and characterized by a set of corresponding parameters: ε_0^i , v^i , Δ^i and w^i , where $i = \text{I, II, III and IV}$, and two angles θ_a^i and θ_b^i which

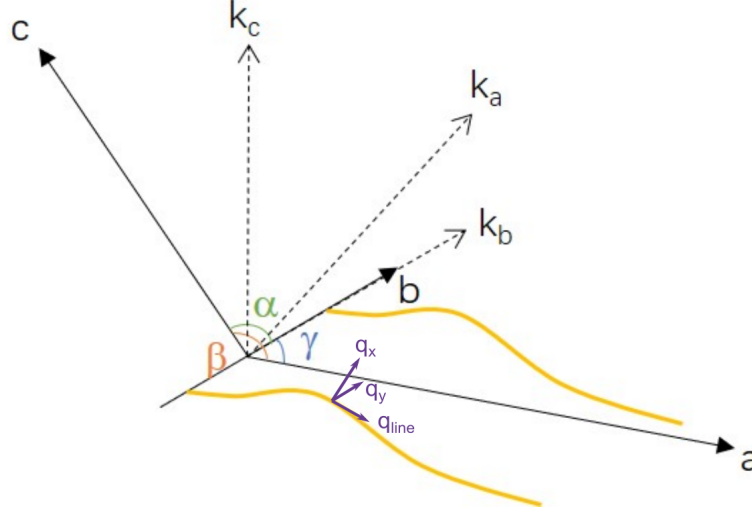


FIG. S2. The position of two nodal lines in NbAs₂ with respect to the real space crystal axes a, b, c and the corresponding reciprocal space axes k_a, k_b, k_c . The local axes along the nodal line: \mathbf{q}_{line} is parallel to the nodal line and $\mathbf{q}_{x,y}$ is always orthogonal to it.

encodes the local direction of the given segment τ^i with respect to a and b crystallographic axes, cf. Figs. S3d,f. Within each segment, these parameters are supposed to be constant except Δ^{III} which we consider to vary linearly with q_{line} to ensure the continuity of the nodal line in energy.

With such simplifications, the diagonal component of optical conductivity is obtained by integration along the chosen segment i , using the local basis of the Hamiltonian:

$$\Re[\sigma_{xx}^i(\omega)] = \frac{Ne^2}{8h} \int dq_{\text{line}} \left(1 + \frac{4(\Delta^i)^2}{(\hbar\omega)^2} \right) [f(\epsilon_0^i + \hbar w^i q_{\text{line}} - \hbar\omega/2) - f(\epsilon_0^i + \hbar w^i q_{\text{line}} + \hbar\omega/2)] \Theta(\hbar\omega - 2\Delta^i) \quad (\text{S2})$$

and, by the isotropy of the model, $\sigma_{xx}^i(\omega) = \sigma_{yy}^i(\omega)$. The other diagonal component reads:

$$\Re[\sigma_{zz}^i(\omega)] = \frac{Ne^2}{4h(v^i)^2} \int dq_{\text{line}} \left(\frac{\partial \Delta^i}{\partial q_{\text{line}}} \right)^2 \left[1 - \left(\frac{\Delta^i}{\hbar\omega} \right)^2 \right] [f(\epsilon_0^i + \hbar w^i q_{\text{line}} - \hbar\omega/2) - f(\epsilon_0^i + \hbar w^i q_{\text{line}} + \hbar\omega/2)] \Theta(\hbar\omega - 2\Delta^i). \quad (\text{S3})$$

In the equations above, $N = 2$ is the number of the nodal lines in the Brillouin zone (double degeneracy due to spin already included), f is the Fermi-Dirac distribution and Θ is the Heaviside function. The main contribution to the optical conductivity comes from Eq. (S2). Eq. (S3) leads to a non-zero contribution to optical conductivity only when the gap parameter changes with q_{line} . Such a possibility is not explicitly included in the Hamiltonian (S1), nevertheless, as mentioned above, it is relevant in our approximation for the segment III (see Fig. S3b). Anyway, in practice, the contribution from (S3) is negligible due to the small ratio between $\hbar^{-1} \partial_{q_{\text{line}}} \Delta^i$ and v^i .

In our reflectivity measurements at $B = 0$ (Fig. 1d top in the main text), the incident radiation was polarized linearly along the a or b axes. So, to calculate the experimentally probed optical conductivities $\Re[\sigma_{aa}(\omega)]$ and $\Re[\sigma_{bb}(\omega)]$, one has to make a corresponding projection for each segment ($i = \text{I, II, III and IV}$) and sum their contributions:

$$\Re[\sigma_{aa}(\omega)] = \sum_i (\cos^2 \theta_a^i \Re[\sigma_{zz}^i(\omega)] + \sin^2 \theta_a^i \Re[\sigma_{xx}^i(\omega)]) \quad (\text{S4})$$

$$\Re[\sigma_{bb}(\omega)] = \sum_i (\cos^2 \theta_b^i \Re[\sigma_{zz}^i(\omega)] + \sin^2 \theta_b^i \Re[\sigma_{xx}^i(\omega)]). \quad (\text{S5})$$

Even though we use a relatively crude approximation for the profile of the nodal lines, there still remains a number of free parameters to be tuned/set. For each segment, we have its length k_i in momentum space, four Hamiltonian parameters v^i , Δ^i , w^i and ϵ_0^i , two angles θ_a and θ_b . The Fermi energy is an additional parameter common to all segments. To reduce this number, let us consider the following points: (i) When the anisotropy of the dispersion

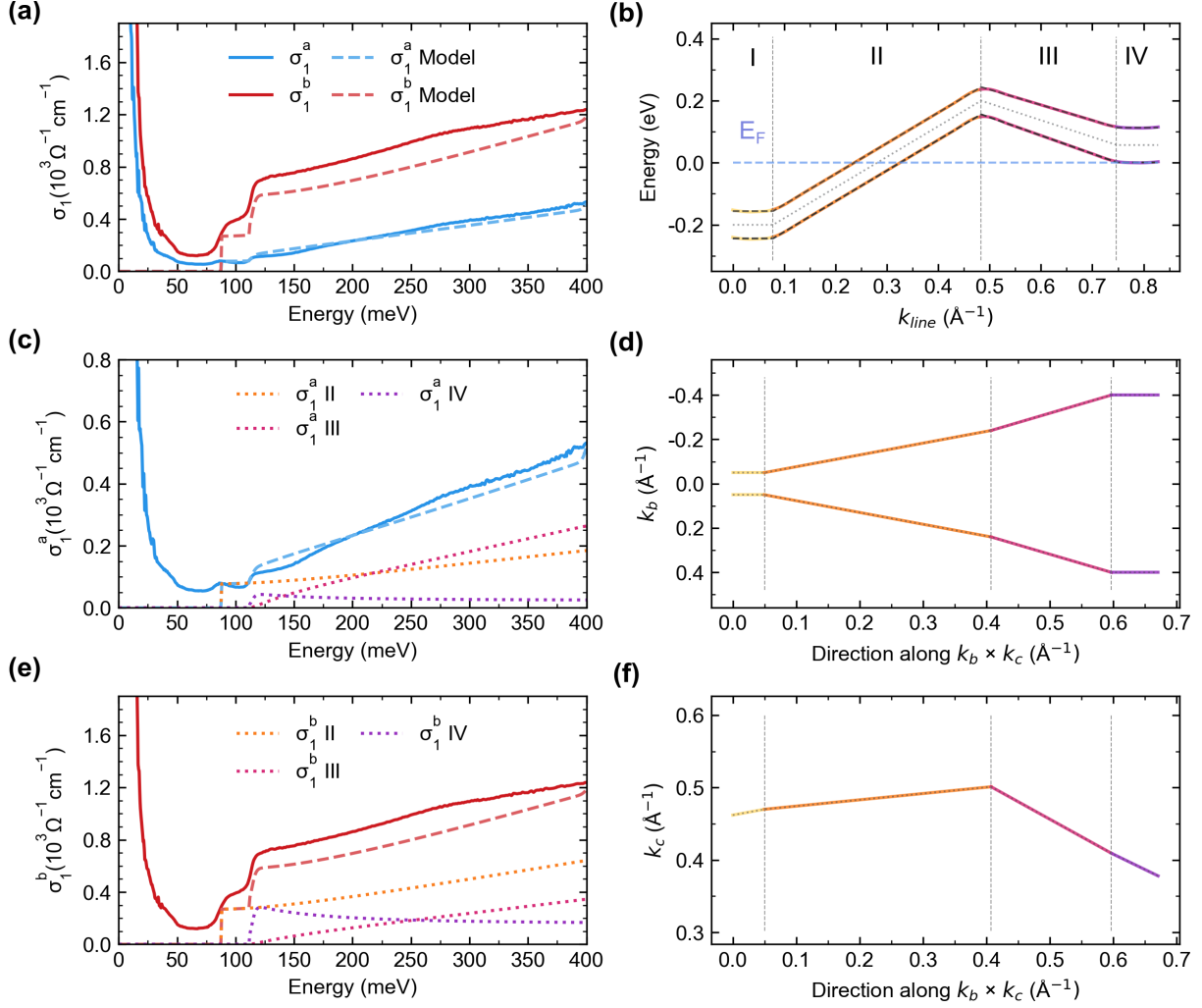


FIG. S3. Parts (a),(c) and (e): Real part of optical conductivity (solid lines) deduced via Kramers-Kronig analysis of the NbAs₂ reflectivity response measured on the (001)-oriented facet at $T = 10$ K using radiation polarized linearly along the a and b crystallographic axes. The dashed and dotted lines show results of theoretical modelling described in the text. Parts (b), (d) and (f): Energy (at \mathbf{k}_{line}) and momentum profiles of the nodal lines considered in the simplified (segment-based) model for optical conductivity of NbAs₂ at $B = 0$.

perpendicular to the nodal line is neglected (i.e., $v_x^i = v_y^i$), the main contribution to optical conductivity (S2) becomes independent of the velocity parameter v^i . (ii) For the parameters Δ^i and w^i as well as the corresponding angles, θ_a^i and θ_b^i , for $i = \text{II}$ and IV , we have solid estimates coming from the analysis of the magneto-optical response, due to the dispersive and flat parts of the nodal line, respectively: e.g., $\Delta^{\text{II}} = \Delta_D$, $\Delta^{\text{IV}} = \Delta_F$, $w^{\text{II}} = w$, $w^{\text{IV}} = 0$. (iii) Additional constraints on w^i , Δ^i , ε_0^i and k^i , appear because the nodal lines are continuous in momentum as well as in energy. For instance, the size of the Brillouin zone approximately fixes the sum of segments lengths and the gap parameter Δ^{III} has to evolve smoothly from $\Delta^{\text{II}} = \Delta_F$ to $\Delta^{\text{IV}} = \Delta_D$. In the latter case, we choose the simplest linear in q_{line} approximation. (iv) The expected profile of the nodal line [1] allows us to neglect – due to Pauli occupation effect – the contribution of interband excitations coming from the segment I. This is because we are only interested in the optical response at relatively low photon energies (below $\hbar\omega \approx 400$ meV, see Fig. S3a).

Using the constraints (i) to (iv), the number of freely tunable parameters is strongly reduced, basically down to the segments' lengths. The theoretically calculated conductivity approaches fairly well the experimentally measured curves, see Fig. S3a. The contributions of individual segments are shown using dotted lines and the corresponding color coding in Figs. S3c,e. Notably, the agreement could be further improved by considering velocity anisotropy ($v_x^i \neq v_y^i$) which alters the relative strength of individual segments. Such an approach has been successfully used by

Shao et al. [1], nevertheless, we prefer not introducing (three) additional tuning parameters which cannot be directly determined from our magneto-optical experiments.

The obtained values of the used tuning parameters – the lengths of the segments k^i and the angles θ_a^{III} and θ_b^{III} – are visualized graphically in Figs. S3d,f in which the nodal line location was projected to the (a - c) and (b - c) crystallographic planes, respectively. Let us remind that the vectors \mathbf{k}_b and $\mathbf{k}_b \times \mathbf{k}_c$ lies in the a - b plane while the vectors \mathbf{k}_c , \mathbf{k}_a as well as $\mathbf{k}_b \times \mathbf{k}_c$ lie in the a - c crystallographic plane, see Fig. S2.

III. NODAL LINES IN MAGNETIC FIELD

To model a nodal line subjected to an externally applied magnetic field, we use the (zero-field) Hamiltonian introduced, together with all its parameters, in the main text:

$$\hat{H} = (\varepsilon_0 + \hbar w q_{\text{line}}) \mathbb{1} + \begin{bmatrix} \Delta & \hbar v(q_x - iq_y) \\ \hbar v(q_x + iq_y) & -\Delta \end{bmatrix}, \quad (\text{S6})$$

where we consider only one spin sector (spin up) of one of the two nodal lines ($\xi = +1$) [cf. Eq. (S1)]. The calculations for spin down or the other nodal line follow exactly the same procedure as we are about to show below.

A. Landau levels

The Hamiltonian (S6) is isotropic in the x - y plane, hence, we may set, with no loss of generality, that $\mathbf{B} = B(\cos \theta \mathbf{e}_{\text{line}} + \sin \theta \mathbf{e}_x) = B\mathbf{e}_B$ for $0 < \theta < \pi/2$ and define a new orthogonal basis with the third component aligned with the magnetic field:

$$\{\mathbf{e}_{x'}, \mathbf{e}_{y'}, \mathbf{e}_{z'} \equiv \mathbf{e}_B\} = \{\cos \theta \mathbf{e}_x - \sin \theta \mathbf{e}_{\text{line}}, -\mathbf{e}_y, \cos \theta \mathbf{e}_{\text{line}} + \sin \theta \mathbf{e}_x\}. \quad (\text{S7})$$

When this new basis is used, the Hamiltonian reads:

$$H = \hbar w (q_B \cos \theta - q_{x'} \sin \theta) + \hbar v (q_{x'} \cos \theta + q_B \sin \theta) \sigma_x - \hbar v q_{y'} \sigma_y + \Delta \sigma_z, \quad (\text{S8})$$

and our goal is to find the spectrum in the presence of a magnetic field.

Let us first illustrate the relativistic properties embedded in the above Hamiltonian, which will inspire the solution of the problem. When the dispersion along the direction of the magnetic field is neglected ($q_B = 0$), the Hamiltonian becomes that of a tilted 2D massive Dirac electron

$$H = \hbar w q_{x'} \sin \theta + \hbar v q_{x'} \cos \theta \sigma_x - \hbar v q_{y'} \sigma_y + \Delta \sigma_z, \quad (\text{S9})$$

where the tilt velocity along the x' direction is $w \sin \theta$ and the Fermi velocity along the x' and y' directions are $v \cos \theta$ and $-v$, respectively. However, this Hamiltonian is not that for the Lorentz-invariant Dirac equation but a variant of it due to the tilt term. The relativistic properties are revealed once the magnetic field is introduced using the standard Landau gauge, $\mathbf{A} = -By' \mathbf{e}_{x'}$, so that

$$H - \hbar w q_{x'} \sin \theta = -\hbar w \sin \theta eBy' + \hbar v \cos \theta (q_{x'} - eBy') \sigma_x - \hbar v q_{y'} \sigma_y + \Delta \sigma_z, \quad (\text{S10})$$

where one can identify an effective electric field $Bw \sin \theta$ in the y' direction. Most importantly, the right hand side is now that of the standard Lorentz invariant Dirac equation except the anisotropy of the speed of light in the x' and y' directions. Therefore, one encounters now the problem of a relativistic 2D massive Dirac electron in the presence of an electric field of $Bw \sin \theta$ in the y' direction and a magnetic field of B in the z' direction, thus moving with a drift velocity of $w \sin \theta$ in the x' direction assuming a small drift velocity. Remark that the speed of light in the x' direction is replaced by $v \cos \theta$, so the rapidity is defined as $\beta = w \tan \theta / v$. It is well-known in the theory of special relativity that one can always shut down the electric field in the co-moving frame of an electron subjected to a crossed electric and magnetic field if the drift velocity is smaller than the speed of light, i.e., $\beta < 1$ [2, 3]. Working in the co-moving frame, with the drift velocity, and using a Lorentz boost, the problem is thus simplified to that of an electron subjected only to magnetic field, i.e., the usual Landau quantization problem. Once one finds the Landau levels (LL) in the co-moving frame, the spectrum in the lab frame, i.e., the original frame of reference, follows immediately by doing the inverse Lorentz boost from the co-moving frame back to the lab frame. Technically, this can be conveniently accomplished using hyperbolic transformation, which is the 2D representation of Lorentz boost in the Lorentz group.

In our case, the hyperbolic transformation of the aforementioned Lorentz boost reads $M = \exp(\phi\sigma_x/2)$, with the rapidity $\beta = \tanh\phi = \omega \tan\theta/v$.

Now we are ready to solve the problem described the Hamiltonian below

$$H = \hbar w [q_B \cos\theta - (q_{x'} - eBy') \sin\theta] + \hbar v [(q_{x'} - eBy') \cos\theta + q_B \sin\theta] \sigma_x - \hbar v q_{y'} \sigma_y + \Delta \sigma_z, \quad (\text{S11})$$

where the magnetic field is already incorporated by the above Landau gauge. Using the same hyperbolic transformation, $M = \exp(\phi\sigma_x/2)$, with the rapidity $\beta = \tanh\phi = w \tan\theta/v$, we obtain the Hamiltonian

$$H_T = M H M \\ = \hbar \frac{wv}{v^*} q_B + \hbar \frac{w^2 + v^2}{v^*} q_B \sin\theta \cos\theta \sigma_x + \hbar v^* (q_{x'} - eBy') \sigma_x - \hbar v q_{y'} \sigma_y + \Delta \sigma_z \quad (\text{S12})$$

where the velocity v^* is defined as

$$v^{*2} = v^2 \cos^2\theta - w^2 \sin^2\theta \quad \text{with} \quad \gamma = \frac{1}{\sqrt{1-\beta^2}} = \cosh\phi = \frac{v \cos\theta}{v^*} \quad (\text{S13})$$

where $\gamma > 1$ is the relativistic Lorentz factor.

Note that H_T does not have the same spectrum as H for the reason that we are now working in the co-moving frame. In the basis of $|\psi_T\rangle = \gamma^{-1/2} M^{-1} |\psi\rangle$ given the eigenstate $|\psi\rangle$ of H , one can construct from H_T another Hamiltonian $H_E = (H_T - E \sinh\phi\sigma_x)/\cosh\phi$ with the same spectrum as H

$$H_E = \frac{\hbar w q_B}{\cos\theta} + \frac{1}{\gamma} \begin{bmatrix} \Delta & \hbar \frac{\sqrt{2vv^*}}{\ell_B} a_E^\dagger \\ \hbar \frac{\sqrt{2vv^*}}{\ell_B} a_E & -\Delta \end{bmatrix} \quad (\text{S14})$$

where $\ell_B = \sqrt{\hbar/(eB)}$ is the magnetic length and a pair of energy-dependent ladder operators is defined as:

$$a_E = -\frac{1}{\sqrt{2vv^*}} \left(\frac{v^*}{\ell_B} (y' - \langle y' \rangle_E) + i\ell_B v q_{y'} \right) \\ a_E^\dagger = -\frac{1}{\sqrt{2vv^*}} \left(\frac{v^*}{\ell_B} (y' - \langle y' \rangle_E) - i\ell_B v q_{y'} \right) \\ \langle y' \rangle_E = \frac{\ell_B^2}{v^*} \left(v^* q_{x'} + q_B \frac{w^2 + v^2}{v^*} \sin\theta \cos\theta - E \frac{w \sin\theta}{\hbar v^*} \right) \quad (\text{S15})$$

with $[a_E, a_E^\dagger] = 1$. The subscript E indicates the dependence on energy E . In particular, the center of cyclotron $\langle y' \rangle_E$ shifts with energy.

Since the energy-dependent term in H_E is absorbed in the definition of the ladder operators, the energy spectrum is self-consistently found in the eigenstates of energy E_n^λ in the form

$$|\psi_{T,n,\lambda}\rangle = \begin{pmatrix} \cos\zeta_{n,\lambda} |n, E_n^\lambda\rangle \\ \sin\zeta_{n,\lambda} |n-1, E_n^\lambda\rangle \end{pmatrix} \quad (\text{S16})$$

where $\zeta_{n,\lambda}$ is an angle depending on n and the sign of energy $\lambda = \pm$, $|n', E_n^\lambda\rangle$ is the wave function of the one-dimensional quantum harmonic oscillator defined by the previous ladder operators. Given the Landau level index n , $n' = n$ or $n-1$.

Finally, we obtain the LL spectrum:

$$E_n^\pm = \hbar w q_B / \cos\theta \pm \sqrt{(\Delta/\gamma)^2 + 2n\hbar e B v^2 \cos\theta / \gamma^3} \quad \text{for } n > 0 \\ E_0 = \hbar w q_B / \cos\theta + \frac{\Delta}{\gamma} \quad \text{for } n = 0, \quad (\text{S17})$$

which has the form typical of massive Dirac electrons, nevertheless, with the gap and velocity renormalized by the pseudo-relativistic Lorentz factor: $2\Delta \rightarrow 2\Delta/\gamma$ and $v^2 \rightarrow v^2/\gamma^3$. Importantly, for the other line index $\xi = -1$ or the spin down we obtain an analogous LL spectrum replacing Δ by $-\Delta$.

It is worth noting that the discussed Lorentz-boost-driven renormalization of the apparent band gap may, to certain extent, resemble the well-known Franz-Keldysh effect [4, 5] which finds its practical use in electro-optical modulation, see e.g. Ref. [6]. Even a closer analogy appears when the Franz-Keldysh effect is explored in crossed electric and magnetic fields [7]. Nevertheless, in our case, there is no real electric field applied to the explored system. It only appears in an effective way, in the pseudo-relativistic Dirac-type Hamiltonian, being proportional to the magnetic-field component perpendicular to $\boldsymbol{\tau}_D$.

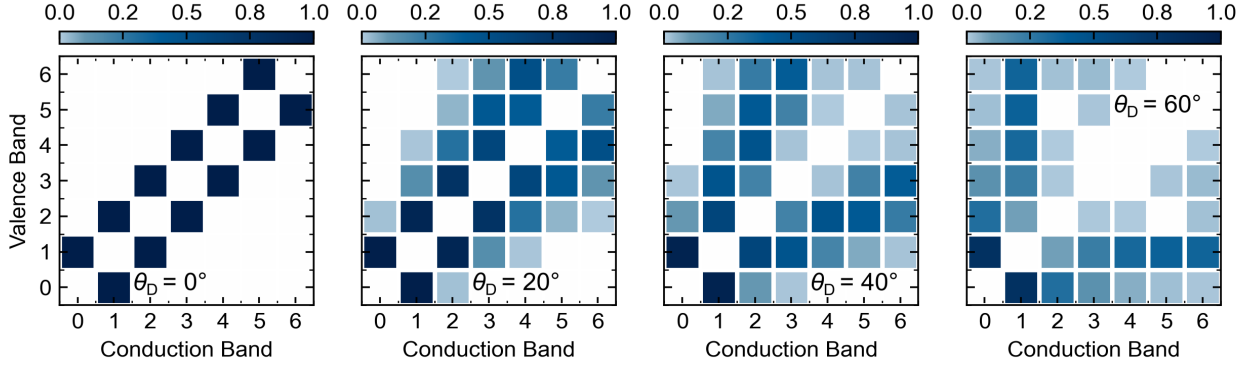


FIG. S4. Relative strength of inter-band transitions between different pairs of Landau levels (for $n = 0 \dots 6$) plotted for angles $\theta_D = 0, 20, 40, 60^\circ$, and parameters (w , v_D and Δ_D) deduced experimentally for the dispersive part of the nodal line in NbAs₂. For $\theta_D = 0^\circ$, we obtain standard selection rules $n \rightarrow n \pm 1$ for electric-dipole transitions, typical of all isotropic systems. With increasing θ_D , gradually, additional transitions become allowed ($n \rightarrow n \pm 2, \pm 3 \dots$). For large angles θ_D , but still for $\beta < 1$, one finds a plethora of optically active transitions. The dominant ones follow the rule-of-thumb selection rules $n \rightarrow \alpha n$ and $n \rightarrow n/\alpha$, where α is an integer ($\alpha = 2 - 4$ for $\theta_D = 60^\circ$).

B. Velocity operators

To study the magneto-optical properties of NbAs₂ theoretically, one has to evaluate the matrix element of the corresponding velocity operators: $\langle \psi_n | \hat{v}_{\mathbf{k}} | \psi_m \rangle$. In this case, it is more practical to work with the basis $|\psi_{T,n}\rangle$ already in hands by remarking that

$$\langle \psi_n | \nabla_{\mathbf{k}} H | \psi_{n'} \rangle = \gamma \langle \psi_{T,n} | \nabla_{\mathbf{k}} H_T | \psi_{T,n'} \rangle \quad (\text{S18})$$

thanks to the fact that M is k -independent. So, in the basis $|\psi_T\rangle$, the velocity operators for H_T are

$$\hat{v}_{T,x} = v^* \sigma_x \quad (\text{S19})$$

$$\hat{v}_{T,y} = -v \sigma_y \quad (\text{S20})$$

$$\hat{v}_{T,z} = \frac{wv}{v^*} + \frac{w^2 + v^2}{v^*} \sin \theta \cos \theta \quad (\text{S21})$$

where one notices an emergent anisotropy of the velocity parameter induced by the applied magnetic field.

C. Selection rules

With the velocity operators, one can *a priori* derive the selection rules for electric-dipole inter-LL transitions which are active in the Faraday configuration (the configuration with the wave vector of light parallel to B). We proceed in a way analogous Landau-quantized tilted 3D cones [3]. When calculating the matrix elements such as $\langle \psi_{T,n} | \hat{v}_{T,x} | \psi_{T,m} \rangle$, one has to deal with terms such as $\langle n', E_n | m', E_m \rangle$ which are no longer 0 or 1. This is due to the mismatch of their energy-dependent orbital center [see Eq. (S15)]. Therefore, we do not obtain, in general, the selection rules, $n \rightarrow n \pm 1$, typical of isotropic solids [8]. Instead, all direct transitions become in principle possible, as long as the occupation of states (Pauli principle) allows. The transitions stemming from the selection rule other than $n \rightarrow n \pm 1$ proliferates in the optical conductivity. By the sum rule, this would dilute the prominent Landau fan which reflects the $n \rightarrow n \pm 1$ rule. Therefore, the usual clear-cut Landau fan is blurred.

To illustrate the evolution of electric-dipole selection rules with the angle θ_D between the magnetic field and the local nodal-line direction of the dispersive part $\boldsymbol{\tau}$, we proceed in the way analogous to [3] and [9]. In Fig. S4, we plot normalized squares of matrix elements, such as $|\langle \psi_{T,n} | \hat{v}_{T,x} / v^* | \psi_{T,m} \rangle|^2$, for different interband inter-LL excitations (for indices $n = 0 \dots 6$) and parameters deduced for the dispersive part of the nodal line in NbAs₂. As expected, one obtains the standard selection rules in isotropic systems for $\theta_D = 0^\circ$: $n \rightarrow n \pm 1$. This is because the energy-dependence in the cyclotron center is canceled by $\sin \theta$ [see in Eq. (S15)]. For non-zero, but small angles θ_D , the magneto-optical response is still dominated by $n \rightarrow n \pm 1$ transitions, although other excitations emerge as well (*e.g.*, $n \rightarrow n \pm 2$). In contrast, for larger angles θ_D , one finds a plethora of optical transitions. The dominant ones follow the

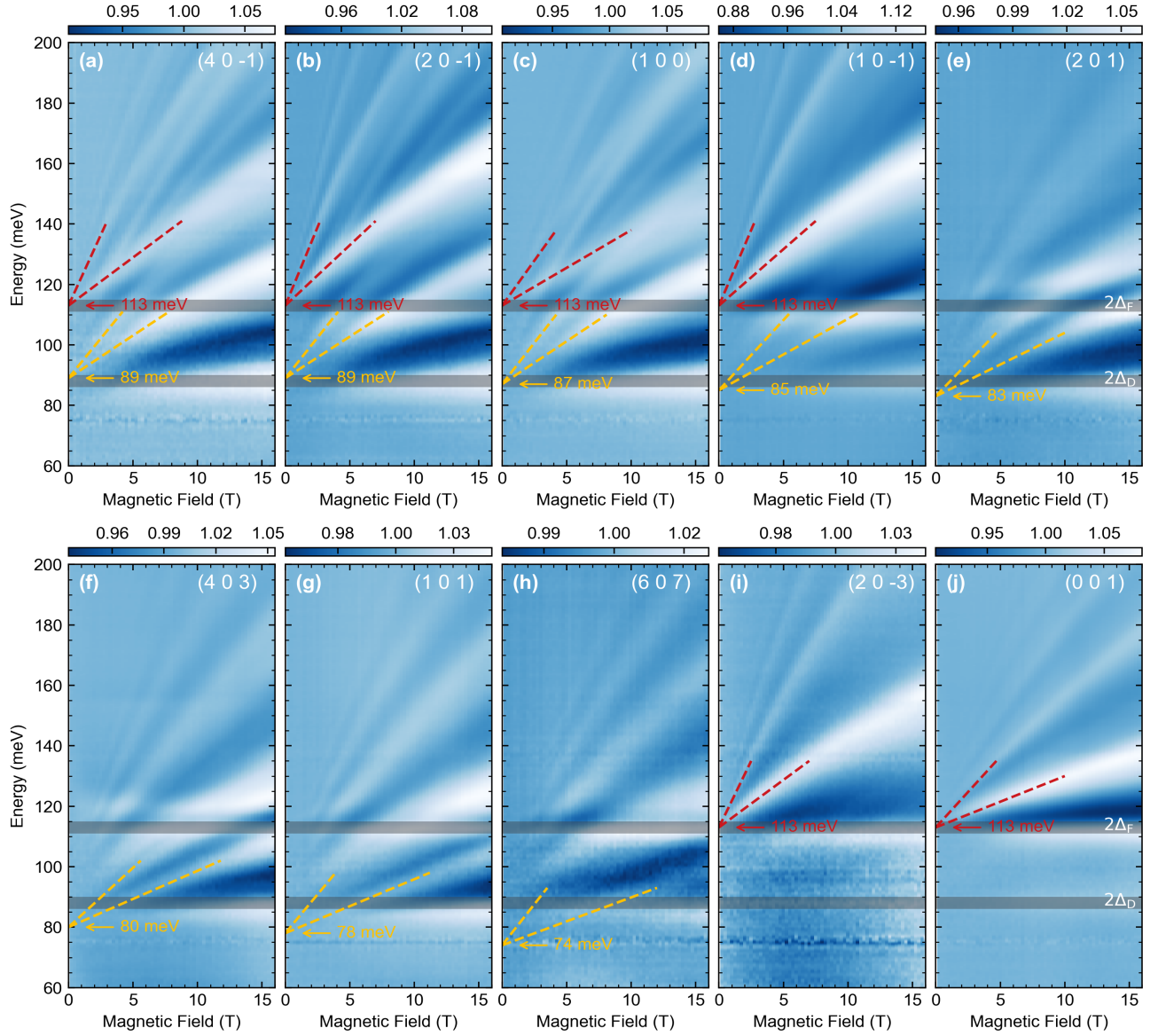


FIG. S5. Parts (a-j): Relative magneto-reflectivity of NbAs₂, R_B/R_0 , in the magnetic field applied perpendicular to ten different crystallographic planes: (40 $\bar{1}$), (20 $\bar{1}$), (100), (10 $\bar{1}$), (201), (403), (101), (607), (20 $\bar{3}$) and (001), which make angles 12, 7, 29, 39, 51, 58, 63, 65, 56 and 90° with the a crystallographic axis, respectively. Horizontal gray bars correspond to positions of two steps in the onset of interband excitations at $2\Delta_D$ and $2\Delta_F$ at $B = 0$, cf. Fig. 1d in the main text or Fig. S3. The yellow and red values indicate the apparent band gap, $2\Delta_D^{\text{eff}}$ and $2\Delta_F$, deduced using a linear zero-field extrapolation of inter-LL resonance belonging to the lower and upper sets (yellow and red dashed lines), respectively.

rule-of-thumb selection rules $n \rightarrow \alpha n$ and $n \rightarrow n/\alpha$, where α is an integer ($\alpha = 4 - 6$ in the right panel of Fig. S4), in agreement with preceding works on tilted 3D cones [2, 3]. This result may be viewed in a broader context of materials which do not have a full rotational symmetry along the direction of the applied magnetic field and in which inter-LL excitations beyond the basic selection rules $n \rightarrow n \pm 1$ become electric-dipole active [10, 11].

IV. INFRARED MAGNETO-REFLECTIVITY TECHNIQUE AND COMPLEMENTARY MAGNETO-OPTICAL DATA

The magneto-reflectivity of NbAs₂ was explored in the Faraday configuration, with \mathbf{B} applied perpendicular to the chosen crystallographic plane. During experiments, a macroscopic area of the sample (typically a few mm²), placed in a superconducting coil and kept at $T = 4.2$ K in the helium exchange gas, was exposed to radiation of a globar, which was analyzed by the Vertex 80v Fourier-transform spectrometer and delivered to the sample via light-pipe optics. The reflected light was detected by a liquid-helium-cooled bolometer placed outside the magnet. The reflectivity R_B recorded at a given magnetic field B was normalized by $R_{B=0}$. To facilitate the data analysis, we assumed that the maxima in relative magneto-reflectivity, R_B/R_0 , directly correspond to the positions of inter-LL resonances. This is justified when the imaginary part of the dielectric function exceeds the absolute value of the real part – a condition fulfilled at photon energies around and slightly above the plasma edge (Fig. 1d). A more detailed analysis indicates that, in this way, we slightly overestimate/underestimate the positions of resonances at lower/higher part of the explored range.

In total, we have explored the magneto-optical response of NbAs₂ with B applied perpendicular to ten different crystallographic planes. The false-color plots of R_B/R_0 for the (101), (201), (100), (20 $\bar{1}$) and (001) planes are presented in the main part of the manuscript (Fig. 2). A complete set of false-colour plots, which include the results collected on all explored facets, is presented in Fig. S5. The corresponding stack-plots of R_B/R_0 spectra are plotted in Fig. S6, except for the (20 $\bar{1}$) and (001) facets presented in the main part of our manuscript (Fig. 2). Let us note that the explored NbAs₂ monocrystals did not have sufficiently large (101) and (607) facets that would allow us to collect magneto-optical data with a sufficiently high quality. Therefore, we used a larger-in-size (403) facet on Sample 1 rotated respectively by 5° and 7°.

To analyze the magneto-reflectivity data quantitatively, we used the procedure described in the main text. We have focused on the lowest observed line in both sets and assign it to the inter-LL excitation $0 \leftrightarrow 1$ and extracted the effective value of the gap $2\Delta^{\text{eff}}$ and velocity v^{eff} using the formula:

$$\hbar\omega_{0\leftrightarrow 1} = \Delta^{\text{eff}} + \sqrt{(\Delta^{\text{eff}})^2 + 2e\hbar B(v^{\text{eff}})^2}. \quad (\text{S22})$$

The extracted values of $2\Delta^{\text{eff}}$ and velocity v^{eff} were then plotted for flat and dispersive parts/crossings in Figs. 3a,b and c,d, respectively, in the main part of the manuscript. Notably, for certain facets, inter-LL transitions belonging only to one of two sets are observed. For the upper set, originating in the flat part of the nodal line, this happens for angles θ_F approaching $\pi/2$ and nearly vanishing perpendicular field component $B \cos \theta_F$. This is the case, for instance of the (607) crystallographic plane (Fig. S5h) with $\theta_F \approx 90^\circ$. In contrast, the lower set of inter-LL excitations – stemming from the dispersive part of the nodal line – vanishes at significantly lower angles θ_D , due to Lorentz-boost-driven collapse of the LL spectrum. For instance, the lower set of excitations is completely missing in the response measured with B applied perpendicular to the (203) plane, see Fig. S5i, for which $\theta_D \approx 64^\circ$.

V. MAGNETO-TRANSPORT EXPERIMENTS

Magneto-transport experiments provided us with another, complementary characterization of the explored NbAs₂ crystals. To this end, we have chosen a monocrystal from the same batch as Sample 1. The electrical contacts were deposited using silver paint in the corners of the (001)-oriented facet of a rectangular shape. The current was always applied along b axis of the sample and the longitudinal magneto-resistance R_{xx} measured at selected (low) temperatures. Two sets of experiments were performed, with the magnetic field applied perpendicular to the a - b plane and along the a axis, see Figs. S7a and b, respectively. In both cases, a pronounced magneto-resistance $R_{xx}(B)$ was observed [12]. Shubnikov-de Haas oscillations became visible in the background removed data ΔR_{xx} . The corresponding fast Fourier-transform applied to $\Delta R_{xx}(1/B)$ implies several characteristic oscillation frequencies and harmonics, see Figs. S7c and d. While the frequency $F_a \approx 300$ T seems to be rather independent of the magnetic field direction, other frequencies, F_b and F_c , indicate a large degree of anisotropy and correspondingly non-spherical Fermi surfaces. The damping of oscillations with temperature has been used to get estimates of the effective (cyclotron) masses m^* . The damping of the most prominent frequencies, i.e., $F_a = 276$ T and $F_c = 120$ T for the magnetic field applied perpendicular to the (001) plane and $F_a = 280$ T with B parallel to the a axis, was analyzed using Lifshitz-Kosevich formula:

$$\Delta_0/\Delta(T_0) = \frac{\alpha T m^*/\bar{B}}{\sinh(\alpha T m^*/\bar{B})}, \quad (\text{S23})$$

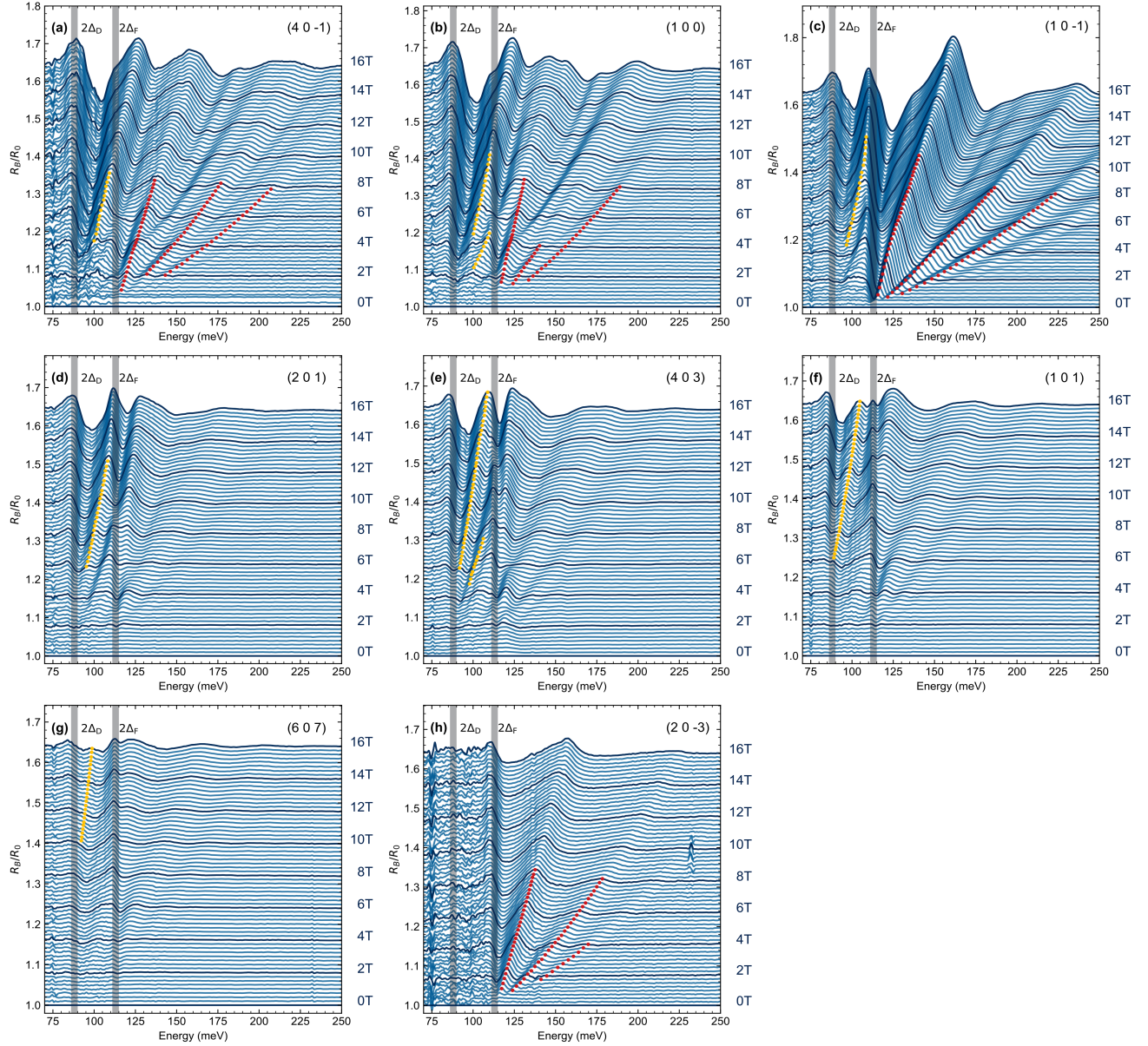


FIG. S6. Parts (a-j): Waterfall plots of relative magneto-reflectivity spectra of NbAs₂, R_B/R_0 , in the magnetic field applied perpendicular to eight different crystallographic planes: $(40\bar{1})$, (100) , $(10\bar{1})$, (201) , (403) , (101) , (607) and $(20\bar{3})$, which make angles 12, 29, 39, 51, 58, 63, 65 and 56° with the a crystallographic axis, respectively. Vertical gray bars correspond to positions of two steps in the onset of interband excitations at $2\Delta_D$ and $2\Delta_F$ at $B = 0$, cf. Fig. 1d in the main text or Fig. S3. The yellow and red points identify maxima of inter-LL resonances belonging to the upper and lower sets at low magnetic fields, respectively.

where \bar{B} stands for the mean magnetic field, T_0 is the lowest measured temperature and $\alpha = 2\pi^2 k_B m_0 / (e\hbar) = 14.69$ T/K. The fitted effective masses are similar for all three frequencies $m^* = (0.25 \pm 0.05)m_0$ where m_0 is the bare electron mass. This result is in agreement with values reported in the literature [12–15].

To explore this (an)isotropy in greater detail, we followed the longitudinal magneto-resistance of NbAs₂ as a function of the magnetic-field direction with respect to the crystal, while keeping the current flowing along the b axis. In Figs. S7e,f, the magnetic field was applied perpendicular to the a and b axes and the sample rotated around the a and b crystallographic axes, respectively. In the latter case, the frequencies F_b and F_c exhibit a fairly pronounced angle dependence, with the maximum appearing roughly at $\theta_{B,a} \approx 90^\circ$ (i.e., $B \perp a$) and with the maximum-to-minimum

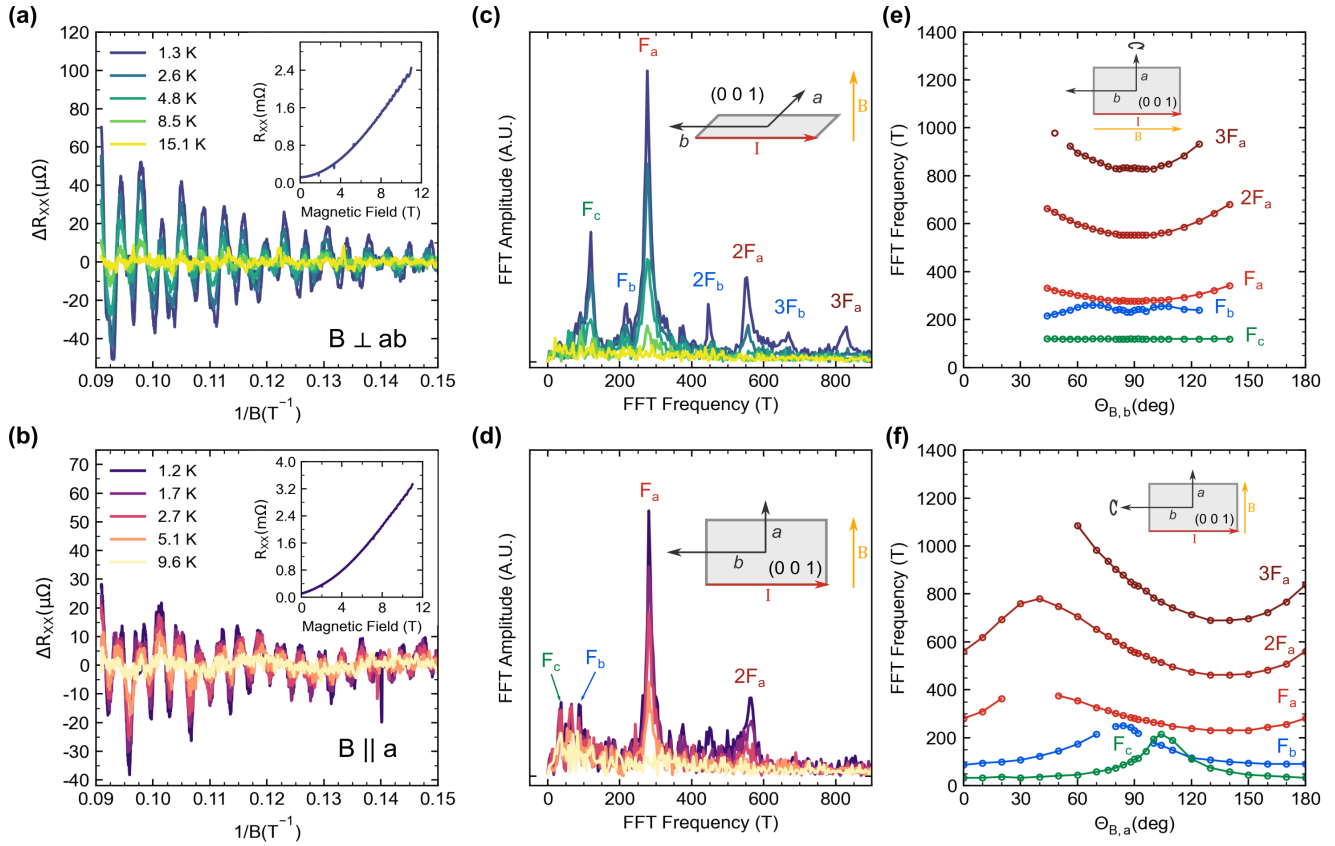


FIG. S7. Parts (a) and (b): Longitudinal magneto-resistance, R_{xx} and $\Delta R_{xx}(B)$, measured at indicated temperatures. The corresponding Fourier-transform applied $\Delta R_{xx}(1/B)$ are plotted in parts (c) and (d): together with insets showing the directions of the magnetic field and current. Parts (e) and (f): Sh-dH oscillation frequencies measured at $T = 1.5$ K as a function of the angle θ between the magnetic field and the b and a axes, respectively, see insets.

ratio reaching nearly 10. This indicates strongly elongated, cigar-like, Fermi surfaces oriented approximately along the a axis. In contrast, the frequencies F_b and F_c remain nearly constant when rotating the sample around the a axis. Such behavior agrees with conclusions of the preceding magneto-transport studies [12–15], and importantly, also with the presence of the nodal lines propagating roughly parallel to the a crystallographic axis.

-
- [1] Y. Shao, Z. Sun, Y. Wang, C. Xu, R. Sankar, A. J. Breindel, C. Cao, M. M. Fogler, A. J. Millis, F. Chou, Z. Li, T. Timusk, M. B. Maple, and D. N. Basov, Optical signatures of Dirac nodal lines in $NbAs_2$, PNAS **116**, 1168 (2019).
 - [2] S. Tchoumakov, M. Civelli, and M. O. Goerbig, Magnetic-field-induced relativistic properties in type-I and type-II Weyl semimetals, Phys. Rev. Lett. **117**, 086402 (2016).
 - [3] J. Sári, M. O. Goerbig, and C. Töke, Magneto-optics of quasirelativistic electrons in graphene with an inplane electric field and in tilted Dirac cones in $\alpha - (BEDT \text{ TTF})_2I_3$, Phys. Rev. B **92**, 035306 (2015).
 - [4] W. Franz, Einfluß eines elektrischen Feldes auf eine optische Absorptionskante, Zeitschrift für Naturforschung A **13**, 484 (1958).
 - [5] L. V. Keldysh, Behavior of non-metallic crystals in strong electric fields, Soviet Journal of Experimental and Theoretical Physics **6**, 763 (1958).
 - [6] K. Liu, C. R. Ye, S. Khan, and V. J. Sorger, Review and perspective on ultrafast wavelength-size electro-optic modulators, Laser & Photonics Reviews **9**, 172 (2015).
 - [7] A. G. Aronov and G. E. Pikus, Light absorption in semiconductors in crossed electric and magnetic fields, Soviet Physics JETP **24**, 339 (1967).
 - [8] G. Landwehr and E. I. Rashba, *Landau level spectroscopy* (Elsevier, 2012).
 - [9] The technical trick to analytically evaluate the matrix element is described in the Supplementary information of [2] or

- in [16].
- [10] M. Orlita, P. Neugebauer, C. Faugeras, A.-L. Barra, M. Potemski, F. M. D. Pellegrino, and D. M. Basko, Cyclotron motion in the vicinity of a Lifshitz transition in graphite, *Phys. Rev. Lett.* **108**, 017602 (2012).
 - [11] O. Ly and D. M. Basko, Theory of electron spin resonance in bulk topological insulators Bi_2Se_3 , Bi_2Te_3 and Sb_2Te_3 , *J. Phys.: Condens. Matter* **28**, 155801 (2016).
 - [12] Z. Yuan, H. Lu, Y. Liu, J. Wang, and S. Jia, Large magnetoresistance in compensated semimetals TaAs_2 and NbAs_2 , *Phys. Rev. B* **93**, 184405 (2016).
 - [13] B. Shen, X. Deng, G. Kotliar, and N. Ni, Fermi surface topology and negative longitudinal magnetoresistance observed in the semimetal NbAs_2 , *Phys. Rev. B* **93**, 195119 (2016).
 - [14] Y.-Y. Wang, Q.-H. Yu, P.-J. Guo, K. Liu, and T.-L. Xia, Resistivity plateau and extremely large magnetoresistance in NbAs_2 and TaAs_2 , *Phys. Rev. B* **94**, 041103 (2016).
 - [15] G. Peramaiyan, R. Sankar, I. P. Muthuselvam, and W.-L. Lee, Anisotropic magnetotransport and extremely large magnetoresistance in NbAs_2 single crystals, *Sci. Rep.* **8**, 1 (2018).
 - [16] M. O. Scully, M. S. Zubairy, *et al.*, Quantum optics cambridge university press, Cambridge, CB2 2RU, UK (1997).